8-2011

Particle Trajectories in Wall-Normal and Tangential Rocket Chambers

Ajay Katta
akatta@utk.edu

To the Graduate Council:

I am submitting herewith a thesis written by Ajay Katta entitled "Particle Trajectories in Wall-Normal and Tangential Rocket Chambers." I have examined the final electronic copy of this thesis for form and content and recommend that it be accepted in partial fulfillment of the requirements for the degree of Master of Science, with a major in Aerospace Engineering.

Joseph Majdalani, Major Professor

We have read this thesis and recommend its acceptance:

Trevor M. Moeller, Christian G. Parigger

Accepted for the Council:
Carolyn R. Hodges

Vice Provost and Dean of the Graduate School

(Original signatures are on file with official student records.)

To the Graduate Council:

I am submitting herewith a thesis written by Ajay Katta entitled "Particle Trajectories in Wall-Normal and Tangential Rocket Chambers." I have examined the final electronic copy of this thesis for form and content and recommend that it be accepted in partial fulfillment of the requirements for the degree of Master of Science, with a major in Aerospace Engineering.

_____

Joseph Majdalani, Major Professor

We have read this thesis

and recommend its acceptance:

_____

Trevor M. Moeller

_____

Christian G. Parigger

Accepted for the Council

_____

Carolyn R. Hodges

Vice Provost and Dean of the Graduate School

PARTICLE TRAJECTORIES IN WALL -NORMAL AND TANGENTIAL INJECTION ROCKET CHAMBERS

A Thesis Presented for

the Master of Science

The University of Tennessee, Knoxville

Ajay Katta

August 2011

Acknowledgments

First, I would like to thank my advisor, Dr. Joe Majdalani for his support and guidance throughout this thesis work. I am also grateful for the financial support provided by the MABE department, UTSI. I would like to extend my gratitude to my committee members: Dr. Christian Parigger and Dr. Trevor Moeller. I thank them for taking the time to mentor me throughout my degree. I would like to thank my friends Jason Howison and Brian Maicke for helping me in improving my work.

Personally, I would like to thank my parents and friends for their constant support and encouragement. Finally, I wish to acknowledge all of those who have guided me toward the completion of my Master of Science degree.

Abstract

The focus of this study is the prediction of trajectories of solid particles injected into either a cylindrically- shaped solid rocket motor (SRM) or a bidirectional vortex chamber (BV). The Lagrangian particle trajectory is assumed to be governed by drag, virtual mass, Magnus, Saffman lift, and gravity forces in a Stokes flow regime. For the conditions in a solid rocket motor, it is determined that either the drag or gravity forces will dominate depending on whether the sidewall injection velocity is high (drag) or low (gravity). Using a one-way coupling paradigm in a solid rocket motor, the effects of particle size, sidewall injection velocity, and particle-to-gas density ratio are examined. The particle size and sidewall injection velocity are found to have a greater impact on particle trajectories than the density ratio. Similarly, for conditions associated with a bidirectional vortex engine, it is determined that the drag force dominates. Using a one-way particle tracking Lagrangian model, the effects of particle size, geometric inlet parameter, particle-to-gas density ratio, and initial particle velocity are examined. All but the initial particle velocity are found to have a significant impact on particle trajectories. The proposed models can assist in reducing slag retention and identifying fuel injection

configurations that will ensure proper confinement of combusting droplets to the inner vortex in solid rocket motors and bidirectional vortex engines, respectively.

Table of Contents

List of Figures

Nomenclature

m_p	=	mass of the solid inert particle
$\boldsymbol{v}$	=	particle velocity
$\boldsymbol{r}$	=	position vector that is general function of space
$\boldsymbol{u}$	=	velocity of flow
$\boldsymbol{e}_r, \boldsymbol{e}_\theta, \boldsymbol{e}_z$	=	cylindrical unit vectors in a curvilinear coordinate system
P	=	pressure
D	=	diameter of solid particle
u_r	=	velocity component of flow in radial direction
u_θ	=	velocity component of flow in tangential direction
u_z	=	velocity component of flow in axial direction
μ	=	coefficient of viscosity of gas
T_{rr}	=	normal stress acting on the particle
$T_{r\theta}$	=	shear stress acting on the particle

$\boldsymbol{F_D}$	=	drag force
C_D	=	coefficient of drag
Re_r	=	relative Reynolds number, $D\lvert u-v\rvert\rho_f \,/\, \mu$
f	=	drag factor, $C_D \,\mathrm{Re}_r / 24$
U	=	relative velocity between fluid and particle
C_m	=	coefficient of added mass
V_p	=	volume of particle
D	=	diameter of particle
a	=	chamber radius
b	=	chamber outlet radius
A_i	=	chamber outlet radius
$r,\ z$	=	normalized radial and axial coordinates, $\overline{r} \,/\, a$, $\overline{z} \,/\, a$
l	=	chamber aspect ratio
S	=	swirl number, $\pi ab \,/\, A$
$\bar{Q}_i$	=	inlet volumetric flow rate
Q_i	=	normalized volumetric flow rate, $\bar{Q}_i \,/\, (Ua^2)$

Greek

ψ	=	stream function

Φ	=	potential function
ρ_p	=	density of particle
ρ_f	=	density of flow
σ	=	modified swirl number, $Q_i^{-1} = S \,/\, (\pi\beta)$
κ	=	inflow parameter, $Q_i \,/\, (2\pi l) = (2\pi\sigma l)^{-1}$

Chapter 1

Introduction

The focus of this study is to predict the trajectories of solid particles entrained in either a bidirectional vortex (BV) chamber [1] or a cylindrically-shaped solid rocket motor (SRM). This is accomplished by carefully evaluating the various forces that can potentially affect the motion of designated particles that simulate the secondary liquid or solid phase in particular configurations of liquid and solid rockets. The term particle is therefore used to denote either liquid droplets (fuel, oxidizer, or mixture) and/or solid particulates.

The particles considered in this investigation are assumed to be chemically inert with a sufficiently small Stokes number to the extent of justifying the use of a one-way coupling paradigm. Accordingly, the effect of particle scattering on the primary fluid phase may be neglected [2]. Furthermore, the particle loading fraction is taken to be sufficiently small to mitigate the effects of particle-particle interactions [3]. With these assumptions at hand, a detailed analysis of the various forces [4] that may affect particle

trajectory will be carried out in the context of both a liquid-liquid vortex engine and a solid rocket motor. In this effort, the effect of initial particle velocity, position, and density on the forces and particle trajectory will be examined.

One of the objectives of this study is to better understand the two-phase flow motion in vortex engines and cylindrical rocket motors. Generally speaking, multiphase flows can be classified based on the particular phase in question and its components such as gas-solid, gas-liquid, and solid-liquid flows [5]. As such, the characterization of multiphase flows has broad applications outside the area of propulsion. Examples include unbounded flows in meteorology and astrophysics where attention is directed to the prediction of weather patterns. These include hurricanes (tropical cyclones), typhoons, dust devils, sand storms, water spouts, galactic pinwheels, and so on [6]. They may also include bounded flows such as those arising in industrial applications where Lagrangian

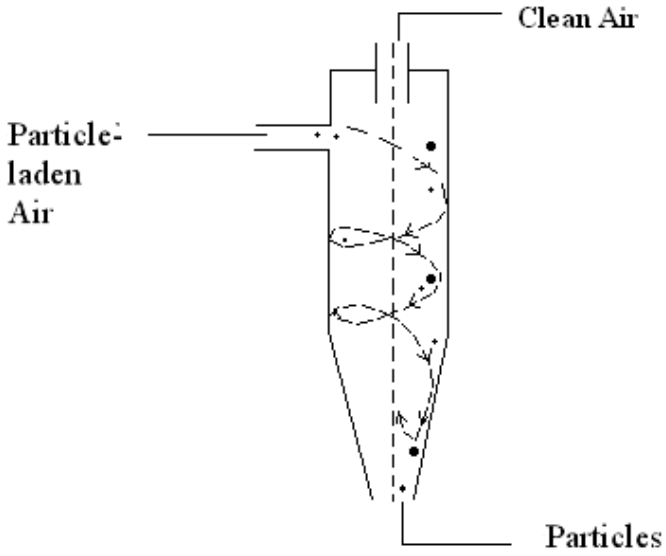

Figure 1-1 Sketch of a cyclone separator.

particle tracking are needed. These encompass the modeling of fluidized beds [7], cyclone separators (illustrated in Figure 1-1), thermal sprays [8] (see Figure 1-2), aerosols [9], fire extinguishers, aluminum particle entrainment in solid rocket motors [10], and oxidizer/fuel droplet dispersion in liquid rocket engines [11]. Clearly, multiphase flows appear in almost every conceivable phenomenon encountered in industry and nature alike.

In the propulsion community, the characterization of powdered aluminum fuel in solid rocket motors (SRMs) that contain aluminum oxides (alumina) has been an ongoing endeavor since the 1980s. These studies are prompted by the need to understand the factors leading to the significant accumulation of slag in SRM submerged nozzles and the erosion of rocket nozzles caused by the impingement of alumina (e.g., ATK Thiokol's SRM [12] shown in Figure 1-3). To this end, several investigations have been carried out with the aim of characterizing slag accumulation and nozzle erosion. By way of example,

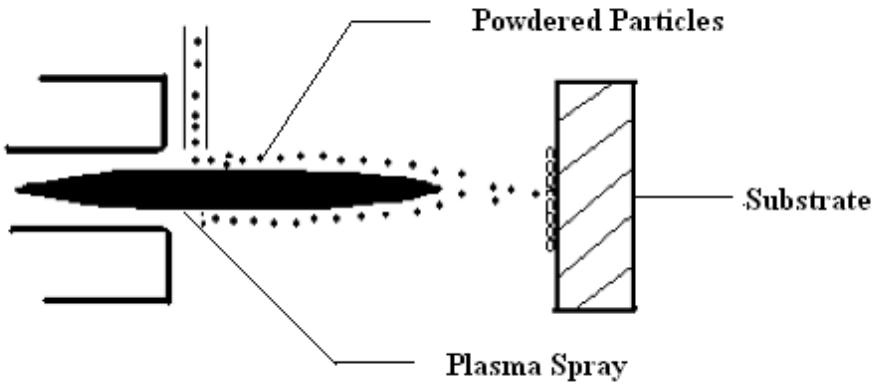

Figure 1-2 Schematic of plasma spray.

one may mention work by Boraas [13], Neilson [14], Haloulakos [15], and others. In most solid propellants, typical aluminum particle loading averages 20% by mass and range in size distribution from 5 to 200 μm in diameter. There are several known advantages to aluminum-based additives. By embedding aluminum particles in solid propellants, the amount of heat release is increased by 20% [16], thereby increasing the specific impulse and overall rocket performance. Horton and McGie [17] and also Price [18] have shown that adding aluminum particles suppresses high frequency combustion instabilities, especially those arising in the transverse direction. However, although aluminum increases the performance of SRMs, the slag retention in the submerged nozzle can be detrimental to the performance and control of the motor. Other concerns regarding alumina and slag formation in SRMs include penalties in vehicle inert weight, reduction in total impulse because of multiphase flow interactions, drag, and uncertainties in thermal insulation. Even to this day, detailed studies of two-phase flows in SRMs are

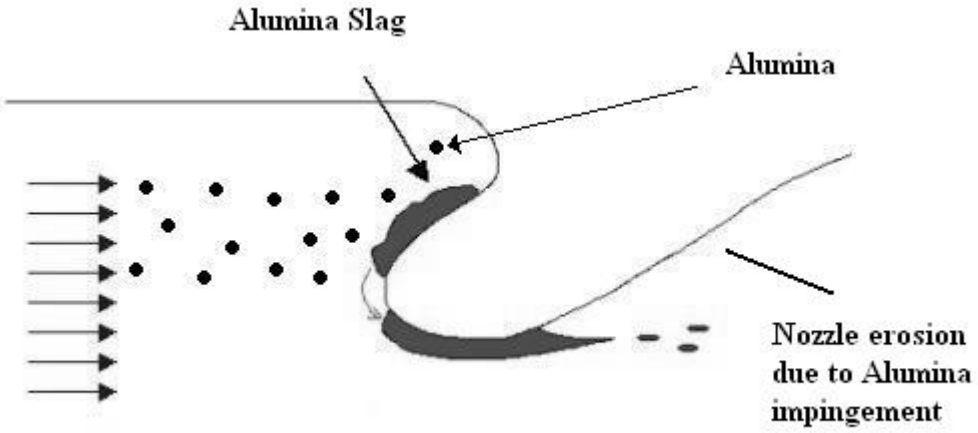

Figure 1-3 Alumina slag and nozzle erosion in solid rocket motors due to combustion of aluminum particles.

often simplified to the extent that numerous thermophysical parameters are either assumed or ignored in two-phase flow investigations involving particle-particle interactions and particle-wall interactions [19].

The modeling of particle motion in swirling flows has received equal attention because of its various applications in industry. These include oil refineries [20], cement processing, coal-fired gas turbine flows [21], sewage treatment, and dust collectors [22]. Swirling flows have also been employed in several propulsive applications including the so-called Vortex Combustion Cold Wall Chamber (VCCWC) by Chiaverini et al. [23] (see Figure 1-4). The cyclonic flow motion in this combustion device offers unique advantages such as the ability to reduce engine cooling requirements by utilizing the low temperature oxidizer stream entering the chamber as a film coolant. While former studies have shown that the combustion of gaseous oxidizer and fuel streams will remain confined to the inner vortex core [24], the conditions leading to the confinement of liquid droplets to the inner chamber region have not been established yet. In this vein, it is the purpose of this study to investigate the conditions leading to droplet entrainment and migration, thus helping to identify injection configurations that would ensure the proper confinement of droplets and the avoidance of wall impingement. Clearly, the distribution of combusting droplets along the walls will lead to undesirable “hot spots” that must be prevented. So while a Lagrangian particle trajectory study in a vortex chamber constitutes an important parameter in engine design, it does not appear to have been studied yet.

Modeling of particle trajectories can be carried out using one of two methodologies. The first consists of a Lagrangian or trajectory tracking approach and the

second, of a two-fluid or Eulerian-Eulerian approach [25]. In the latter, particles are treated as a second fluid with suitable conservation equations, whereas, in the former, each particle is treated individually. When taken individually, each of the specific mass, velocity, and temperature of each particle is calculated separately. In a strictly multiphase flow environment, one must also consider the motion around the particles, the mass transfer between phases, particle-particle interactions, and particle-wall interactions. The ensuing calculations can hence become computationally intensive depending on the flow regime and turbulence model used.

In this study the particle loading will be assumed to be sufficiently low to justify the use of a Lagrangian approach in modeling flow trajectories. This will be applied to

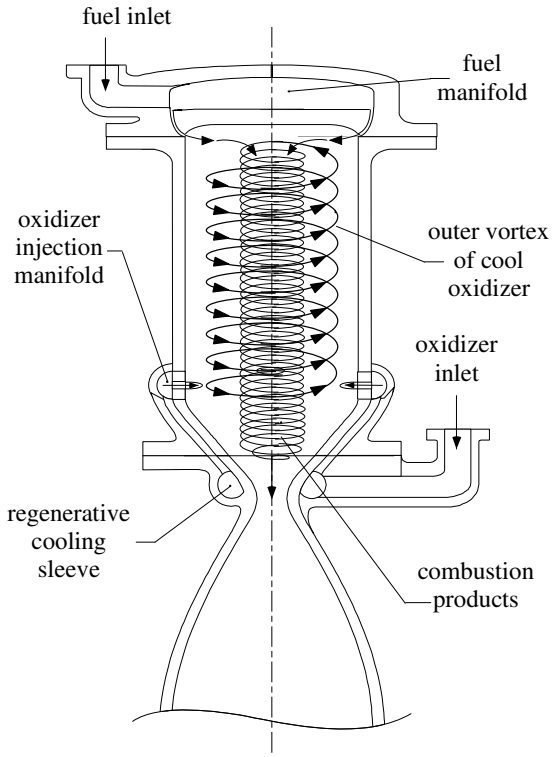

Figure 1-4 Vortex Combustion Cold Wall Chamber (VCCWC) [26].

both an idealized model of the VCCWC and a cylindrically-shaped SRM. To set the stage, a brief introduction to the Lagrangian and Eulerian approaches will be given in Sections 1.1 and 1.2.

1.1 Lagrangian Approach or Trajectory Method

The Lagrangian approach is based on Newton's second law where the particle mass, initial velocity and forces acting on a particle are known. A detailed description of this method is presented in Chapter 2. The basic equation of motion follows, as usual, from Equation 1.1, where the variables are defined in the Nomenclature section.

$$m_p \frac{\mathrm{d}\boldsymbol{v}}{\mathrm{d}t} = \sum \boldsymbol{F} \tag{1.1}$$

where the symbols are defined in the Nomenclature.

1.2 Two-Fluid Modeling

In a two-fluid model, the dispersed phase is treated as a continuum subject to its own conservation equations. Consequently, it is imperative to take into account the mass, momentum and energy transfer between any two phases in order to solve the conservation equations either theoretically or numerically. The detailed derivation of the conservation equations for a carrier phase and a dispersed phase problem are given in Crowe et al. [3]; a summary of these equations is furnished below:

1.2.1 Equations for Carrier or Continuous Phase

Continuity equation:

$$\frac{\partial}{\partial t}\left(\alpha_c \rho_c\right) + \frac{\partial}{\partial x_i}\left(\alpha_c \rho_c u_i\right) = -n\dot{m} \tag{1.2}$$

Momentum equation:

$$\begin{aligned}&\frac{\partial}{\partial t}\left(\alpha_c \rho_c u_i\right) + \frac{\partial}{\partial x_i}\left(\alpha_c \rho_c u_j u_i\right) = -\alpha_c \frac{\partial P}{\partial x_i} + \alpha_c \frac{\partial \tau_{ij}}{\partial x_i} \\ &+\alpha_c \rho_c g_i - \beta_V \left(u_i - v_i\right) - n\dot{m} v_i\end{aligned} \tag{1.3}$$

Thermal energy equation:

$$\begin{aligned}&\frac{\partial}{\partial t}\left(\alpha_c \rho_c i_c\right) + \frac{\partial}{\partial x_i}\left(\alpha_c \rho_c u_i i_c\right) = \frac{\partial}{\partial x_i} k_e \frac{\partial T_c}{\partial x_i} - P \frac{\partial}{\partial x_i}\left(\alpha_d v_i + \alpha_c u_i\right) \\ &+\tau_{ij} \frac{\partial}{\partial x_i}\left(\alpha_d v_i + \alpha_c u_i\right) + \alpha_c \rho_c g_i - \beta_V \left(u_i - v_i\right)^2 + \beta_T \left(T_d - T_c\right) \\ &-n\dot{m}\left(h_s + \tfrac{1}{2}\left|v_i - u_i\right|^2\right) + n\dot{V}_d P_s\end{aligned} \tag{1.4}$$

1.2.2 Equations for Dispersed Phase

Continuity equation:

$$\frac{\partial}{\partial t}\left(\alpha_d \rho_d\right) + \frac{\partial}{\partial x_i}\left(\alpha_d \rho_d v_i\right) = -\frac{\partial}{\partial x_i}\left(D_d \frac{\partial \overline{\rho}_d}{\partial x_i}\right) + n\dot{m} \tag{1.5}$$

Momentum equation:

$$\begin{aligned}&\frac{\partial}{\partial t}\left(\alpha_d \rho_d v_i\right) + \frac{\partial}{\partial x_i}\left(\alpha_d \rho_d v_j v_i\right) = -\alpha_d \frac{\partial P}{\partial x_i} + \alpha_d \frac{\partial \tau_{ij}}{\partial x_j} \\ &+\alpha_d \rho_d g_i - \beta_V \left(u_i - v_i\right) - n\dot{m} v_i\end{aligned} \tag{1.6}$$

Thermal energy equation:

$$\frac{\partial}{\partial t}\left(\alpha_d \rho_d i_d\right) + \frac{\partial}{\partial x_i}\left(\alpha_d \rho_d v_i i_d\right) = -n\dot{E}_\sigma + n\dot{Q}_r + n\dot{m}h_s + \beta_T\left(T_c - T_d\right) - n\dot{V}_d P_s \tag{1.7}$$

In the above, n denotes the number density that defines the number of particles per unit volume, α_c represents the volume fraction of the continous phase, α_d represents the volume fraction of the dispersed phase, and $\overline{\rho}_d$ is the bulk density, which is defined as the mass of the dispersed phase per unit volume of mixture. As mentioned earlier, only the Lagrangian approach was used in this study.

Chapter 2

Problem Formulation

2.1 Particle Velocity and Acceleration

For a solid, passive particle entrained in a gaseous flowfield, Newton's second law can be called upon. In general the motion of an injected particle may be described using

$$m_p \frac{\mathrm{d}\boldsymbol{v}}{\mathrm{d}t} = \sum \boldsymbol{F} \tag{2.1}$$

In cylindrical coordinates, the position vector may be defined as shown in Figure 2-1 [27], namely,

$$\boldsymbol{r} = r\,\boldsymbol{e}_r + z\boldsymbol{e}_z \tag{2.2}$$

Subsequently, the particle velocity may be calculated from

$$\boldsymbol{v} = \frac{\mathrm{d}\boldsymbol{r}}{\mathrm{d}t} = \dot{r}\boldsymbol{e}_r + r\dot{\boldsymbol{e}}_r + \dot{z}\boldsymbol{e}_z + z\dot{\boldsymbol{e}}_z \tag{2.3}$$

Then noting that

$$\dot{\boldsymbol{e}}_r = \dot{\theta}\boldsymbol{e}_\theta \;;\; \dot{\boldsymbol{e}}_\theta = -\dot{\theta}\boldsymbol{e}_r \;;\; \dot{\boldsymbol{e}}_z = 0 \tag{2.4}$$

one obtains

$$\boldsymbol{v} = \dot{r}\boldsymbol{e}_r + r\dot{\theta}\boldsymbol{e}_\theta + \dot{z}\boldsymbol{e}_z \tag{2.5}$$

Using similar differentiation, the acceleration may be derived using

$$\frac{\mathrm{d}\boldsymbol{v}}{\mathrm{d}t} = \ddot{r}\boldsymbol{e}_r + \dot{r}\dot{\boldsymbol{e}}_r + \dot{r}\dot{\theta}\boldsymbol{e}_\theta \;+ r\ddot{\theta}\boldsymbol{e}_\theta + r\dot{\theta}\dot{\boldsymbol{e}}_\theta + \ddot{z}\boldsymbol{e}_z + \dot{z}\dot{\boldsymbol{e}}_z \tag{2.6}$$

$$= \ddot{r}\boldsymbol{e}_r + \dot{r}\dot{\theta}\boldsymbol{e}_\theta \;+ \dot{r}\dot{\theta}\boldsymbol{e}_\theta + r\ddot{\theta}\boldsymbol{e}_\theta - r\dot{\theta}^2\boldsymbol{e}_r \;+ \ddot{z}\boldsymbol{e}_z \tag{2.7}$$

Thus by collecting terms in the same spatial direction, we retrieve:

$$\frac{\mathrm{d}\boldsymbol{v}}{\mathrm{d}t} = \left(\ddot{r} - r\dot{\theta}^2\right)\boldsymbol{e}_r + \left(2\dot{r}\dot{\theta} + r\ddot{\theta}\right)\boldsymbol{e}_\theta + \ddot{z}\boldsymbol{e}_z \tag{2.8}$$

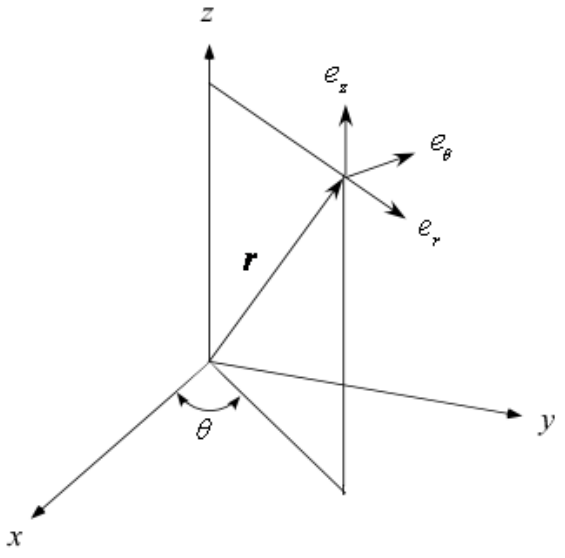

Figure 2-1 Polar cylindrical coordinate system used in this study.

The term $r\dot{\theta}^2$ is sometimes referred to as the centrifugal term, and the term $2\dot{r}\dot{\theta}$ as the Coriolis term [28].

2.1.1 Particle Drag Force

The steady-state drag represents the drag force that acts on the solid particle or the liquid droplet in a uniform pressure field in the absence of relative acceleration between the particle and the conveying fluid. Given the size of the particles, one may assume a Stokes flow regime in which inertia may be ignored in the Navier-Stokes equations [29]. Under such conditions, the momentum equation reduces to

$$\nabla P = \mu \nabla^2 \boldsymbol{u} \tag{2.9}$$

The solution of Eq. (2.9) leads to the Stokes stream function [29] for a sphere of radius a that is moving with relative velocity U. The result is

$$\psi = \frac{U}{2}\left(r^2 + \frac{a^3}{2r} - \frac{3ar}{2}\right)\sin^2\theta \tag{2.10}$$

At the outset, velocity components of the fluid become

$$u_r = U\left(1 + \frac{a^3}{2r^3} - \frac{3a}{2r}\right)\cos\theta \tag{2.11}$$

$$u_\theta = -U\left(1 - \frac{a^3}{4r^3} - \frac{3a}{4r}\right)\sin\theta \tag{2.12}$$

Having determined the velocity, the pressure may be deduced from the radial component of the momentum equation. One gets

$$P = P_\infty - \frac{3\mu U a}{2r^3}\cos\theta \tag{2.13}$$

where P_∞ represents the free stream pressure. Similarly, the normal stress acting on the particle in the radial direction may be estimated from

$$T_{rr} = -P + \sigma_{rr}; \sigma_{rr} = \frac{\partial u_r}{\partial r} \tag{2.14}$$

In our case, $\sigma_{rr} = 0$ along $r = a$, and so the normal stress becomes

$$T_{rr} = -P_\infty + \frac{3\mu U a}{2r^3}\cos\theta \tag{2.15}$$

Similarly, the shear stress on the particle may be calculated from

$$T_{r\theta} = \sigma_{r\theta} \tag{2.16}$$

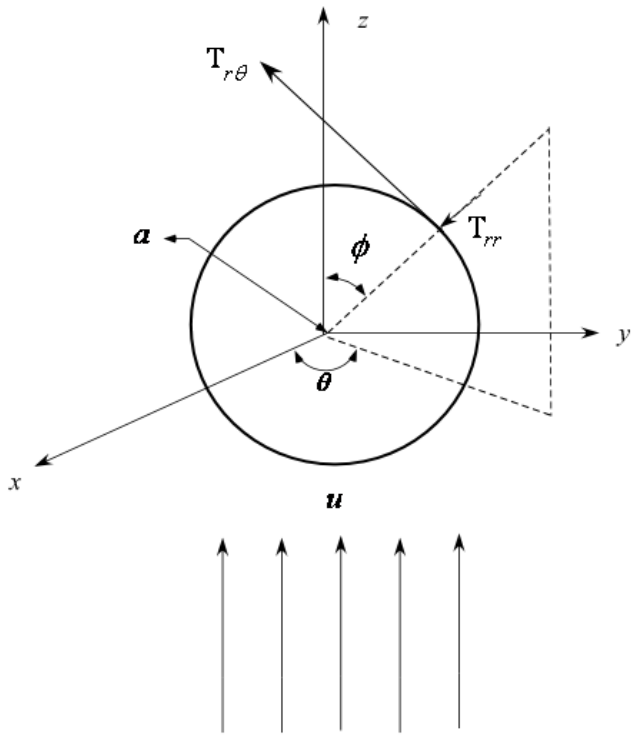

Figure 2-2 Stresses acting on a spherical particle in crossflow.

where

$$T_{r\theta} = \mu\left[r\frac{\partial}{\partial r}\left(\frac{u_\theta}{r}\right) + \frac{1}{r}\frac{\partial u_r}{\partial \theta}\right] = -\frac{3\mu U}{2a}\sin\theta \tag{2.17}$$

As shown in Figure 2-2, the resultant stress on the particle in the z-direction may be used to calculate the Stokes drag on the particle, specifically

$$\boldsymbol{F_D} = \int_0^\pi \left(T_{rr}\cos\theta - T_{r\theta}\sin\theta\right)2\pi a^2 \sin\theta \,\mathrm{d}\theta \tag{2.18}$$

and so

$$\boldsymbol{F}_D = 3\pi\mu DU \tag{2.19}$$

Taking relative velocities into account, the Stokes drag for steady flow past a spherical particle reduces to

$$\boldsymbol{F}_D = 3\pi\mu Df(\boldsymbol{u} - \boldsymbol{v}) \tag{2.20}$$

where f is the drag factor given by

$$f = \frac{C_D \,\mathrm{Re}_r}{24} \tag{2.21}$$

In the above, the relative Reynolds number is based on the absolute relative velocity between fluid and particle. It is written as

$$\mathrm{Re}_r = \frac{D\left|\boldsymbol{u} - \boldsymbol{v}\right|\rho_f}{\mu} \tag{2.22}$$

For Reynolds numbers up to 800, a suitable correlation for the drag factor [30] may be used, namely,

$$f = (1 + 0.15\,\mathrm{Re}_r^{0.687}) \tag{2.23}$$

It should be noted that the analysis so far assumes uniform flow. For non-uniform flow, the drag force must be augmented by the Faxen force [31]. In general vector form, this can be expressed as

$$\boldsymbol{F}_D = 3\pi\mu D f(\boldsymbol{u}-\boldsymbol{v}) + \underbrace{\frac{1}{8}\mu\pi D^3\nabla^2\boldsymbol{u}}_{\text{Faxen force}} \tag{2.24}$$

Based on the above, the drag components in the radial, tangential and axial directions may be evaluated to be

$$F_{D,r} = 3\pi\mu D f(u_r - \dot{r}) + \frac{1}{8}\mu\pi D^3\nabla^2 u_r \tag{2.25}$$

$$F_{D,\theta} = 3\pi\mu D f(u_\theta - r\dot{\theta}) + \frac{1}{8}\mu\pi D^3\nabla^2 u_\theta \tag{2.26}$$

$$F_{D,z} = 3\pi\mu D f(u_z - \dot{z}) + \frac{1}{8}\mu\pi D^3\nabla^2 u_z \tag{2.27}$$

2.1.2 Virtual or Apparent Mass Effect

Generally, when an object is accelerated through a fluid medium, the surrounding fluid, such as a trailing wake, must be accelerated as well. The energy needed to drive the surrounding fluid increases the energy required to accelerate the object, which can be a submerged spherical particle. The energy needed to drive the particle must also drive the wake forming behind it. The inertial force needed to drive the motion of the surrounding fluid is referred to as *apparent* or *virtual mass force*. The additional force needed to accelerate the particle can be determined by assuming a virtual particle mass that is larger than the actual mass. In this context, the apparent force needed to accelerate the particle

(and its wake) may be calculated based on the increased virtual or added particle mass [32]. The magnitude of the added mass is usually determined from the change in kinetic energy of the fluid surrounding an accelerating particle. To see how this calculation may be performed, we first evaluate the total kinetic energy surrounding the particle,

$$\mathrm{KE} = \frac{1}{2}\rho_f \int_V \boldsymbol{u}^2 \mathrm{d}\, V \tag{2.28}$$

where the integral is taken over the entire fluid domain.

The potential function for a sphere of radius a and moving with relative velocity U is simply

$$\Phi = -\frac{a^3}{2r^2} U \cos\theta \tag{2.29}$$

Its corresponding velocity components are

$$u_r = \frac{a^3}{r^3} U \cos\theta \tag{2.30}$$

$$u_\theta = \frac{a^3}{2r^3} U \sin\theta \tag{2.31}$$

As shown in Figure 2-2, one can take an element of volume

$$\Delta V = a\Delta\phi r \Delta\theta \Delta r \tag{2.32}$$

which, in differential form, becomes

$$\mathrm{d}\, V = r^2 \sin\theta \mathrm{d}r\, \mathrm{d}\theta\, \mathrm{d}\phi \tag{2.33}$$

Then given

$$u^2 = u_r^2 + u_\theta^2 \tag{2.34}$$

we can substitute into Eq. (2.28) to get

$$\mathrm{KE} = \frac{1}{2}\rho_f \int_V \boldsymbol{u}^2 \mathrm{d}\,V = \frac{1}{2}\rho_f \int_0^{2\pi}\int_0^{\pi}\int_a^{\infty}\left(u_r^2 + u_\theta^2\right) r^2 \sin\theta \mathrm{d}r\mathrm{d}\theta\mathrm{d}\phi \tag{2.35}$$

$$= \frac{\rho_f U^2 a^6}{2}\int_0^{2\pi}\int_0^{\pi}\int_a^{\infty}\left(\frac{\cos^2\theta}{r^4} + \frac{\sin^2\theta}{4r^4}\right)\sin\theta \mathrm{d}r\mathrm{d}\theta\mathrm{d}\phi$$

$$= \frac{\rho_f U^2 a^6}{2}\int_0^{2\pi}\int_0^{\pi}\left(\frac{\cos^2\theta}{3a^3} + \frac{\sin^2\theta}{12a^3}\right)\sin\theta \mathrm{d}\theta\mathrm{d}\phi$$

$$= \frac{\rho_f U^2 a^3}{6}\int_0^{2\pi}\int_0^{\pi}\left[\cos^2\theta\sin\theta + \frac{1}{4}\left(1-\cos^2\theta\right)\sin\theta\right]\mathrm{d}\theta\mathrm{d}\phi = \frac{1}{3}\rho_f \pi a^3 U^2 \tag{2.36}$$

The work required to change the kinetic energy of the fluid is therefore,

$$\frac{\mathrm{dKE}}{\mathrm{d}t} = \boldsymbol{F}_{vm}\cdot\boldsymbol{U} \tag{2.37}$$

where, for a spherical particle,

$$\boldsymbol{F}_{vm} = \frac{2}{3}\rho_f \pi a^3 U\frac{\mathrm{d}\,\boldsymbol{U}}{\mathrm{d}t} \tag{2.38}$$

and in general

$$\boldsymbol{F}_{vm} = C_m \rho_f V_p \frac{\mathrm{d}\,\boldsymbol{U}}{\mathrm{d}t} \tag{2.39}$$

where C_m is the added mass coefficient and V_p represents the volume of the particle.

The relative acceleration of the fluid with respect to the entrained particle may be expressed as

$$\frac{\mathrm{d}\,\boldsymbol{U}}{\mathrm{d}t} = \frac{\mathrm{d}\boldsymbol{u}(\boldsymbol{r},t)}{\mathrm{d}t} - \frac{\mathrm{d}\boldsymbol{v}(t)}{\mathrm{d}t} \tag{2.40}$$

The virtual mass force acting on a particle becomes

$$\boldsymbol{F}_{vm} = C_m \rho_f V_p \left[\frac{\mathrm{d}\boldsymbol{u}(\boldsymbol{r},t)}{\mathrm{d}t} - \frac{\mathrm{d}\boldsymbol{v}(t)}{\mathrm{d}t} \right] \tag{2.41}$$

The components of force in the radial, tangential and axial directions must be carefully evaluated and expressed as:

$$F_{vm,r} = C_m \rho_f V_p \left[\left(\frac{\partial u_r}{\partial t} + u_r \frac{\partial u_r}{\partial r} + \frac{u_\theta}{r} \frac{\partial u_r}{\partial \theta} + u_z \frac{\partial u_r}{\partial z} - \frac{u_\theta^2}{r} \right) - \left(\ddot{r} - r\dot{\theta}^2 \right) \right] \tag{2.42}$$

$$F_{vm,\theta} = C_m \rho_f V_p \left[\left(\frac{\partial u_\theta}{\partial t} + u_r \frac{\partial u_\theta}{\partial r} + \frac{u_\theta}{r} \frac{\partial u_\theta}{\partial \theta} + u_z \frac{\partial u_\theta}{\partial z} + \frac{u_r u_\theta}{r} \right) - \left(r\ddot{\theta} + 2\dot{r}\dot{\theta} \right) \right] \tag{2.43}$$

$$F_{vm,z} = C_m \rho_f V_p \left[\left(\frac{\partial u_z}{\partial t} + u_r \frac{\partial u_z}{\partial r} + \frac{u_\theta}{r} \frac{\partial u_z}{\partial \theta} + u_z \frac{\partial u_z}{\partial z} \right) - \ddot{z} \right] \tag{2.44}$$

2.1.3 Lift Forces

The lift force acting on particles is mainly caused by two mechanisms. The first is known as the *Magnus force* and may be attributed to particle rotation [33]. The second mechanism is a fluid shearing effect known as the *Saffman lift force* [34].

2.1.3.1 Magnus Force

The Magnus force was first explained by Heinrich Gustav Magnus [33] in 1853. The corresponding lift developed due to the rotation of the particle. Because of the rotation of the particle, higher velocity is induced on one side and lower velocity on the opposite side as shown in Figure 2-3. The resulting asymmetrical pressure distribution

around the particle induces a lift force that tends to move the particle toward the region of higher velocity (or lower pressure). This mechanism is known as the Magnus effect.

In the case of small Reynolds numbers of $O(1)$, Rubinow et al. [35] provide a useful expression for the lift force that can be written as

$$\boldsymbol{F}_{\text{Magn}} = \frac{1}{2}\rho_{\rho} C_L A \left|\boldsymbol{u}-\boldsymbol{v}\right| \left[\frac{\left(\boldsymbol{u}-\boldsymbol{v}\right)\times\boldsymbol{\Omega}_r}{\left(\boldsymbol{\Omega}_d - \frac{1}{2}\nabla\times\boldsymbol{u}\right)}\right] \tag{2.45}$$

where $\boldsymbol{\Omega}_r$ denotes the relative rotation of the particle with respect to the fluid, $\boldsymbol{\Omega}_d$ represents the rotation of the particle, and A refers to the projected area of the particle. The interdependencies comprise:

$$\boldsymbol{\Omega}_r = \boldsymbol{\Omega}_d - \tfrac{1}{2}\nabla\times\boldsymbol{u} \tag{2.46}$$

and

$$C_L = \frac{D\left|\boldsymbol{\Omega}_d\right|}{\left|\boldsymbol{u}-\boldsymbol{v}\right|} \tag{2.47}$$

Because of insufficient detail on particle rotation inside rocket motors, we do not

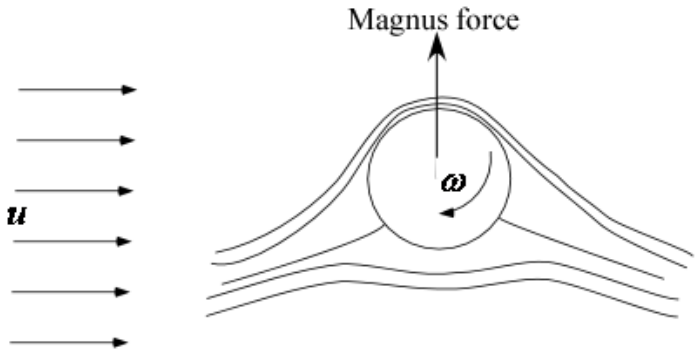

Figure 2-3 Generation of the Magnus force due to particle rotation.

incorporate the Magnus force in our analysis lest an impractical problem is created; however, the Saffman lift force will be accounted for as described in next section.

2.1.3.2 Saffman Lift Force

Figure 2-4 depicts how, for particle motion in sheared flow or near a solid boundary, the velocity gradients in the field produce a lift force known as the Saffman lift force. Saffman analyzed this force [34] for low relative Reynolds numbers Re_r, and small shear Reynolds numbers $\mathrm{Re}_{\mathrm{shear}}$. He found

$$\boldsymbol{F}_{\mathrm{Saff}} = 1.61 D^2 \sqrt{\mu \rho_f \,/\, \left|\nabla \times \boldsymbol{u}\right|} \left[\left(\boldsymbol{u} - \boldsymbol{v}\right) \times \left(\nabla \times \boldsymbol{u}\right)\right] \tag{2.48}$$

where the shear and relative Reynolds numbers are defined as:

$$\mathrm{Re}_{\mathrm{shear}} = \frac{\rho_f D^2}{\mu} \frac{\mathrm{d}u}{\mathrm{d}y} \tag{2.49}$$

(2.50)

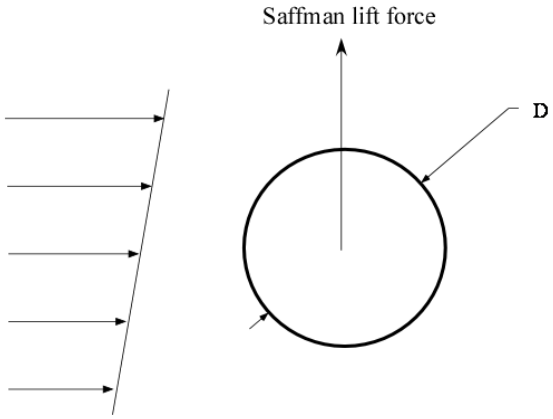

Figure 2-4 Generation of the Saffman lift force in sheared motion.

Here D denotes the particle diameter and y, the direction perpendicular to the flow velocity. In most gas–solid particle flows, the relative Reynolds number does not exceed unity and so the lift force approximation derived by Saffman may be used. Its scalar components in the radial, tangential and axial directions are

$$F_{L,r} = 1.61D^2\sqrt{\mu\rho_f}\left[\left(\frac{1}{r}\frac{\partial u_z}{\partial\theta} - \frac{\partial u_\theta}{\partial r}\right)^2 + \left(\frac{\partial u_r}{\partial z} - \frac{\partial u_z}{\partial r}\right)^2 + \left(\frac{1}{r}\frac{\partial(ru_\theta)}{\partial r} - \frac{1}{r}\frac{\partial u_r}{\partial\theta}\right)^2\right]^{-1/4}$$
$$\times\left[\frac{1}{r}\left(u_\theta - r\dot{\theta}\right)\left(\frac{\partial(ru_\theta)}{\partial r} - \frac{\partial u_r}{\partial\theta}\right) - \left(u_z - \dot{z}\right)\left(\frac{\partial u_r}{\partial z} - \frac{\partial u_z}{\partial r}\right)\right] \quad (2.51)$$

$$F_{L,\theta} = 1.61D^2\sqrt{\mu\rho_f}\left[\left(\frac{1}{r}\frac{\partial u_z}{\partial\theta} - \frac{\partial u_\theta}{\partial r}\right)^2 + \left(\frac{\partial u_r}{\partial z} - \frac{\partial u_z}{\partial r}\right)^2 + \left(\frac{1}{r}\frac{\partial(ru_\theta)}{\partial r} - \frac{1}{r}\frac{\partial u_r}{\partial\theta}\right)^2\right]^{-1/4}$$
$$\times\left[\left(u_z - \dot{z}\right)\left(\frac{1}{r}\frac{\partial u_z}{\partial\theta} - \frac{\partial u_\theta}{\partial z}\right) - \frac{1}{r}\left(u_r - \dot{r}\right)\left(\frac{\partial(ru_\theta)}{\partial r} - \frac{\partial u_r}{\partial\theta}\right)\right] \quad (2.52)$$

$$F_{L,z} = 1.61D^2\sqrt{\mu\rho_f}\left[\left(\frac{1}{r}\frac{\partial u_z}{\partial\theta} - \frac{\partial u_\theta}{\partial r}\right)^2 + \left(\frac{\partial u_r}{\partial z} - \frac{\partial u_z}{\partial r}\right)^2 + \left(\frac{1}{r}\frac{\partial(ru_\theta)}{\partial r} - \frac{1}{r}\frac{\partial u_\theta}{\partial\theta}\right)^2\right]^{-1/4}$$
$$\times\left[\left(u_r - \dot{r}\right)\left(\frac{\partial u_r}{\partial z} - \frac{\partial u_z}{\partial r}\right) - \left(u_\theta - r\dot{\theta}\right)\left(\frac{1}{r}\frac{\partial u_z}{\partial\theta} - \frac{\partial u_\theta}{\partial r}\right)\right] \quad (2.53)$$

2.1.4 Pressure Gradient and Shear Stress in the Conveying Fluid

According to the Archimedes Principle, the pressure force produced by the hydrostatic pressure is equal to the weight per unit volume of the displaced fluid:

$$\boldsymbol{F}_{\text{Arch}} = V_p\left(\nabla P\right) = -\rho_f g V_p \boldsymbol{e}_z = -m_{df} g \boldsymbol{e}_z ; \nabla P = -\rho_f g\, \boldsymbol{e}_z \tag{2.54}$$

where $m_{df}g$ represents the weight of the displaced fluid (i.e. volume of the particle filled by the surrounding fluid). Furthermore, the force on the particle due to the shear stress in the conveying fluid is due to the product of the stress gradient and the volume of the particle,

$$\boldsymbol{F}_{\tau} = \nabla \tau V_p \tag{2.55}$$

The sum of these two forces, normal and tangential, leads to

$$\boldsymbol{F}_{ext} = V_p\left(\nabla \tau - \nabla P\right) \tag{2.56}$$

By considering the equation of motion for an isolated particle, the Navier-Stokes equations for the conveying fluid yield:

$$\rho_f \frac{\mathrm{d}\boldsymbol{u}}{\mathrm{d}t} = \nabla \tau - \nabla P + \rho_f \boldsymbol{g} \; ; \quad \boldsymbol{g} = -g\, \boldsymbol{e}_z \tag{2.57}$$

Note that gravity is taken in the vertical direction. The components of this equation are

$$F_{ext,r} = \rho_f V_p \left(u_r \frac{\partial u_r}{\partial r} + \frac{1}{r} u_\theta \frac{\partial u_r}{\partial \theta} + u_z \frac{\partial u_r}{\partial z} - \frac{u_\theta^2}{r} \right) \tag{2.58}$$

$$F_{ext,\theta} = \rho_f V_p \left(u_r \frac{\partial u_\theta}{\partial r} + \frac{1}{r} u_\theta \frac{\partial u_\theta}{\partial \theta} + u_z \frac{\partial u_\theta}{\partial z} + \frac{u_\theta u_r}{r} \right) \tag{2.59}$$

$$F_{ext,z} = \rho_f V_p \left(u_r \frac{\partial u_z}{\partial r} + \frac{1}{r} u_\theta \frac{\partial u_z}{\partial \theta} + u_z \frac{\partial u_z}{\partial z} - g_z \right) \tag{2.60}$$

2.2 Simplified Equations of Motion for a Single Particle

In obtaining the simplified equations of motion for a single particle we take into account the drag force, lift force, virtual mass effect, pressure gradient and shear stress in the conveying fluid. The total contribution of these forces is summarized below.

By summing up individual contributions, the following equation of motion is arrived at:

$$\rho_p V_p\left(\ddot{r}-r\dot{\theta}\right)=\Bigg\{\underbrace{3\pi\mu Df(u_r-\dot{r})}_{\text{drag term}}+\underbrace{\mu\pi\frac{D^3}{8}(\nabla^2\boldsymbol{u})_r}_{\text{Faxen term}}$$

$$\underbrace{+C_m\rho_f V_p\left[\left(u_r\frac{\partial u_r}{\partial r}+\frac{1}{r}u_\theta\frac{\partial u_r}{\partial\theta}+u_z\frac{\partial u_r}{\partial z}-\frac{u_\theta^2}{r}\right)-\left(\ddot{r}-r\dot{\theta}^2\right)\right]}_{\text{virtual mass term}}$$

$$\underbrace{+\rho_f V_p\left(u_r\frac{\partial u_r}{\partial r}+\frac{1}{r}u_\theta\frac{\partial u_r}{\partial\theta}+u_z\frac{\partial u_r}{\partial z}-\frac{u_\theta^2}{r}\right)}_{\text{pressure and shear term}}$$

$$+1.61D^2\sqrt{\mu\rho_f}\left[\left(\frac{1}{r}\frac{\partial u_z}{\partial\theta}-\frac{\partial u_\theta}{\partial r}\right)^2+\left(\frac{\partial u_r}{\partial z}-\frac{\partial u_z}{\partial r}\right)^2+\left(\frac{1}{r}\frac{\partial(ru_\theta)}{\partial r}-\frac{1}{r}\frac{\partial u_r}{\partial\theta}\right)^2\right]^{-1/4}$$

$$\underbrace{\times\left[\frac{1}{r}\left(u_\theta-r\dot{\theta}\right)\left(\frac{\partial(ru_\theta)}{\partial r}-\frac{\partial u_r}{\partial\theta}\right)-\left(u_z-\dot{z}\right)\left(\frac{\partial u_r}{\partial z}-\frac{\partial u_z}{\partial r}\right)\right]}_{\text{Saffman force term}}\Bigg\} \tag{2.61}$$

This can be rearranged to the extent of separating the highest, second order derivative viz.

$$\ddot{r} = r\dot{\theta}^2 + \frac{1}{\left(\rho_p V_p + C_m \rho_f V_p\right)}\Bigg\{3\pi\mu D f(u_r - \dot{r}) + \mu\pi\frac{D^3}{8}(\nabla^2\boldsymbol{u})_r$$

$$+C_m\rho_f V_p\left(u_r\frac{\partial u_r}{\partial r} + \frac{1}{r}u_\theta\frac{\partial u_r}{\partial\theta} + u_z\frac{\partial u_r}{\partial z} - \frac{u_\theta^2}{r}\right)$$

$$+V_p\left(u_r\frac{\partial u_r}{\partial r} + \frac{1}{r}u_\theta\frac{\partial u_r}{\partial\theta} + u_z\frac{\partial u_r}{\partial z} - \frac{u_\theta^2}{r}\right)$$

$$+1.61D^2\sqrt{\mu\rho_f}\left(\left(\frac{1}{r}\frac{\partial u_z}{\partial\theta} - \frac{\partial u_\theta}{\partial r}\right)^2 + \left(\frac{\partial u_r}{\partial z} - \frac{\partial u_z}{\partial r}\right)^2 + \left(\frac{1}{r}\frac{\partial(ru_\theta)}{\partial r} - \frac{1}{r}\frac{\partial u_r}{\partial\theta}\right)^2\right)^{-1/4}$$

$$\times\left[\frac{1}{r}\left(u_\theta - r\dot{\theta}\right)\left(\frac{\partial(ru_\theta)}{\partial r} - \frac{\partial u_r}{\partial\theta}\right) - \left(u_z - \dot{z}\right)\left(\frac{\partial u_r}{\partial z} - \frac{\partial u_z}{\partial r}\right)\right]\Bigg\} \tag{2.62}$$

Similarly the rearrangement of forces in the tangential direction leads to

$$\ddot{\theta} = -\frac{2\dot{r}\dot{\theta}}{r} + \frac{1}{r\left(\rho_p V_p + C_m\rho_f V_p\right)}\Bigg\{3\pi\mu D f(u_\theta - r\dot{\theta}) + \mu\pi\frac{D^3}{8}(\nabla^2\boldsymbol{u})_\theta$$

$$+C_m\rho_f V_p\left(u_r\frac{\partial u_\theta}{\partial r} + \frac{1}{r}u_\theta\frac{\partial u_\theta}{\partial\theta} + u_z\frac{\partial u_\theta}{\partial z} + \frac{u_\theta u_r}{r}\right)$$

$$+\rho_f V_p\left(u_r\frac{\partial u_\theta}{\partial r} + \frac{1}{r}u_\theta\frac{\partial u_\theta}{\partial\theta} + u_z\frac{\partial u_\theta}{\partial z} + \frac{u_\theta u_r}{r}\right)$$

$$+1.61D^2\sqrt{\mu\rho_f}\left[\left(\frac{1}{r}\frac{\partial u_z}{\partial\theta}-\frac{\partial u_\theta}{\partial r}\right)^2+\left(\frac{\partial u_r}{\partial z}-\frac{\partial u_z}{\partial r}\right)^2+\left(\frac{1}{r}\frac{\partial(ru_\theta)}{\partial r}-\frac{1}{r}\frac{\partial u_r}{\partial\theta}\right)^2\right]^{-1/4}$$

$$\left[\left(u_z-\dot{z}\right)\left(\frac{1}{r}\frac{\partial u_z}{\partial\theta}-\frac{\partial u_\theta}{\partial z}\right)-\frac{1}{r}\left(u_r-\dot{r}\right)\left(\frac{\partial(ru_\theta)}{\partial r}-\frac{\partial u_r}{\partial\theta}\right)\right]\Bigg\} \tag{2.63}$$

Finally, in the axial direction, we get

$$\ddot{z}=\frac{1}{\left(\rho_p V_p+C_m\rho_f V_p\right)}\Bigg\{3\pi\mu Df(u_z-\dot{z})+\mu\pi\frac{D^3}{8}(\nabla^2\boldsymbol{u})_z$$

$$+C_m\rho_f V_p\left(u_r\frac{\partial u_z}{\partial r}+\frac{1}{r}u_\theta\frac{\partial u_z}{\partial\theta}+u_z\frac{\partial u_z}{\partial z}\right)$$

$$+V_p\rho_f\left(u_r\frac{\partial u_z}{\partial r}+\frac{1}{r}u_\theta\frac{\partial u_z}{\partial\theta}+u_z\frac{\partial u_z}{\partial z}\right)$$

$$+1.61D^2\sqrt{\mu\rho_f}\left[\left(\frac{1}{r}\frac{\partial u_z}{\partial\theta}-\frac{\partial u_\theta}{\partial r}\right)^2+\left(\frac{\partial u_r}{\partial z}-\frac{\partial u_z}{\partial r}\right)^2+\left(\frac{1}{r}\frac{\partial(ru_\theta)}{\partial r}-\frac{1}{r}\frac{\partial u_\theta}{\partial\theta}\right)^2\right]^{-1/4}$$

$$\times\left[\left(u_r-\dot{r}\right)\left(\frac{\partial u_r}{\partial z}-\frac{\partial u_z}{\partial r}\right)-\left(u_\theta-r\dot{\theta}\right)\left(\frac{1}{r}\frac{\partial u_z}{\partial\theta}-\frac{\partial u_\theta}{\partial r}\right)\right]\Bigg\} \tag{2.64}$$

2.3 Fourth Order Runge–Kutta Integration

The set of ODEs established in the previous section may be solved using Runge-Kutta integration of fourth order [36]; to do so, the equations are first expressed as a set of first order ODEs of the form

$$\frac{\mathrm{d}y}{\mathrm{d}t}=f\left(t,y\right),\qquad y\left(t_0\right)=y_0 \tag{2.65}$$

This classic technique was developed by C. Runge (1856-1927) and M.W. Kutta (1867-1944). Because only first order differential equations of the type given by Eq. (2.65) can be solved, Runge-Kutta integration can be extended to higher order ODEs after converting them into first order systems. The integration scheme associated with Runge-Kutta integration follows simple, familiar steps. To solve Eq. (2.65), one can write

$$y_{n+1} = y_n + \frac{h}{6}\left(k_1 + 2k_2 + 2k_3 + k_4\right) \tag{2.66}$$

$$t_{n+1} = t + h \tag{2.67}$$

$$\begin{aligned} k_1 &= f\left(t_n, y_n\right) \\ k_2 &= f\left(t_n + \frac{1}{2}h, y_n + \frac{1}{2}hk_1\right) \\ k_3 &= f\left(t_n + \frac{1}{2}h, y_n + \frac{1}{2}hk_2\right) \\ k_4 &= f\left(t_n + h, y_n + hk_3\right) \end{aligned} \tag{2.68}$$

where h is the size of time interval and k_1, k_2, k_3, and k_4 denote the slopes at the beginning, two midpoints, and end of each time interval t_n.

2.4 Numerical Integration of the Coupled ODEs

In order to carefully track particle motion in a gaseous medium characterized by a velocity field vector $\boldsymbol{U}$, the coupled nonlinear ODEs (2.62)–(2.64) must be solved using the Runge-Kutta method described above. Before solving the three coupled second-order ODEs, they must be converted into six first-order equations [37]. To this end, we first express Eqs.(2.62)–(2.64) as

Table 2-1 Set of coupled nonlinear ODEs (2.62)–(2.64)

Variable	Components of forces in three directions
$\ddot{r}$	$= r\dot{\theta}^2 + \frac{1}{\left(\rho_p V_p + C_m \rho_f V_p\right)}\left\{3\pi\mu D f(u_r - \dot{r}) + \mu\pi\frac{D^3}{8}(\nabla^2 \boldsymbol{u})_r + C_m \rho_f V_p\left(u_r \frac{\partial u_r}{\partial r} + \frac{1}{r}u_\theta \frac{\partial u_r}{\partial \theta} + u_z \frac{\partial u_r}{\partial z} - \frac{u_\theta^2}{r}\right)\right.$ $+V_p\left(u_r \frac{\partial u_r}{\partial r} + \frac{1}{r}u_\theta \frac{\partial u_r}{\partial \theta} + u_z \frac{\partial u_r}{\partial z} - \frac{u_\theta^2}{r}\right) + 1.61 D^2 \sqrt{\mu\rho_f}\left(\left(\frac{1}{r}\frac{\partial u_z}{\partial \theta} - \frac{\partial u_\theta}{\partial r}\right)^2 + \left(\frac{\partial u_r}{\partial z} - \frac{\partial u_z}{\partial r}\right)^2 + \left(\frac{1}{r}\frac{\partial (r u_\theta)}{\partial r} - \frac{1}{r}\frac{\partial u_r}{\partial \theta}\right)^2\right)^{-1/4}$ $\left.\times\left[\frac{1}{r}\left(u_\theta - r\dot{\theta}\right)\left(\frac{\partial (r u_\theta)}{\partial r} - \frac{\partial u_r}{\partial \theta}\right) - \left(u_z - \dot{z}\right)\left(\frac{\partial u_r}{\partial z} - \frac{\partial u_z}{\partial r}\right)\right]\right\}$
$\ddot{\theta}$	$= -\frac{2\dot{r}\dot{\theta}}{r} + \frac{1}{r\left(\rho_p V_p + C_m \rho_f V_p\right)}\left\{3\pi\mu D f(u_\theta - r\dot{\theta}) + \mu\pi\frac{D^3}{8}(\nabla^2 \boldsymbol{u})_\theta + C_m \rho_f V_p\left(u_r \frac{\partial u_\theta}{\partial r} + \frac{1}{r}u_\theta \frac{\partial u_\theta}{\partial \theta} + u_z \frac{\partial u_\theta}{\partial z} + \frac{u_\theta u_r}{r}\right)\right.$

Table 2-1 Continued

Variable	Components of forces in three directions
	$+1.61D^2\sqrt{\mu\rho_f}\left[\left(\frac{1}{r}\frac{\partial u_z}{\partial\theta}-\frac{\partial u_\theta}{\partial r}\right)^2+\left(\frac{\partial u_r}{\partial z}-\frac{\partial u_z}{\partial r}\right)^2+\left(\frac{1}{r}\frac{\partial(ru_\theta)}{\partial r}-\frac{1}{r}\frac{\partial u_r}{\partial\theta}\right)^2\right]^{-1/4}+\rho_f V_p\left(u_r\frac{\partial u_\theta}{\partial r}+\frac{1}{r}u_\theta\frac{\partial u_\theta}{\partial\theta}+u_z\frac{\partial u_\theta}{\partial z}+\frac{u_\theta u_r}{r}\right)$ $\times\left[\left(u_z-\dot{z}\right)\left(\frac{1}{r}\frac{\partial u_z}{\partial\theta}-\frac{\partial u_\theta}{\partial z}\right)-\frac{1}{r}\left(u_r-\dot{r}\right)\left(\frac{\partial(ru_\theta)}{\partial r}-\frac{\partial u_r}{\partial\theta}\right)\right]\Bigg\}$
$\ddot{z}$	$=\frac{1}{\left(\rho_p V_p+C_m\rho_f V_p\right)}\Bigg\{3\pi\mu Df(u_z-\dot{z})+\mu\pi\frac{D^3}{8}(\nabla^2\boldsymbol{u})_z+C_m\rho_f V_p\left(u_r\frac{\partial u_z}{\partial r}+\frac{1}{r}u_\theta\frac{\partial u_z}{\partial\theta}+u_z\frac{\partial u_z}{\partial z}\right)$ $+V_p\rho_f\left(u_r\frac{\partial u_z}{\partial r}+\frac{1}{r}u_\theta\frac{\partial u_z}{\partial\theta}+u_z\frac{\partial u_z}{\partial z}\right)+1.61D^2\sqrt{\mu\rho_f}\left[\left(\frac{1}{r}\frac{\partial u_z}{\partial\theta}-\frac{\partial u_\theta}{\partial r}\right)^2+\left(\frac{\partial u_r}{\partial z}-\frac{\partial u_z}{\partial r}\right)^2+\left(\frac{1}{r}\frac{\partial(ru_\theta)}{\partial r}-\frac{1}{r}\frac{\partial u_\theta}{\partial\theta}\right)^2\right]^{-1/4}$ $\times\left[\left(u_r-\dot{r}\right)\left(\frac{\partial u_r}{\partial z}-\frac{\partial u_z}{\partial r}\right)-\left(u_\theta-r\dot{\theta}\right)\left(\frac{1}{r}\frac{\partial u_z}{\partial\theta}-\frac{\partial u_\theta}{\partial r}\right)\right]\Bigg\}$

$$\ddot{r} = f\left(t, r, \dot{r}, \theta, \dot{\theta}, z, \dot{z}\right) \tag{2.69}$$

$$\ddot{\theta} = f\left(t, r, \dot{r}, \theta, \dot{\theta}, z, \dot{z}\right) \tag{2.70}$$

$$\ddot{z} = f\left(t, r, \dot{r}, \theta, \dot{\theta}, z, \dot{z}\right) \tag{2.71}$$

with six suitably posed initial conditions:

$$\begin{array}{l} r\left(t_0\right) = r_0 \;\; ; \dot{r}\left(t_0\right) = \dot{r}_0 \\ \theta\left(t_0\right) = \theta_0 \;\; ; \dot{\theta}\left(t_0\right) = \dot{\theta}_0 \\ z\left(t_0\right) = z_0 \;\; ; \;\; z\left(t_0\right) = \dot{z}_0 \end{array} \tag{2.72}$$

where the subscript "0" denotes initial conditions. Conversion of Eqs. (2.69)–(2.71) into an equivalent first-order system can be achieved by introducing the auxiliary variables:

$$r = y_1 \;\; ; \dot{r} = y_2 \tag{2.73}$$

$$\theta = y_3 \; ; \dot{\theta} = y_4 \tag{2.74}$$

$$z = y_5 \;\; ; \dot{z} = y_6 \tag{2.75}$$

Substituting these variables into Eqs. (2.69)–(2.71) leads to a system of first-order differential equations, specifically

$$\dot{y}_1 = y_2 \tag{2.76}$$

$$\dot{y}_2 = f\left(t, y_1, y_2, y_3, y_4, y_5, y_6\right) \tag{2.77}$$

$$\dot{y}_3 = y_4 \tag{2.78}$$

$$\dot{y}_4 = f\left(t, y_1, y_2, y_3, y_4, y_5, y_6\right) \tag{2.79}$$

$$\dot{y}_5 = y_6 \tag{2.80}$$

$$\dot{y}_6 = f\left(t, y_1, y_2, y_3, y_4, y_5, y_6\right) \tag{2.81}$$

with the same six initial conditions:

$$\begin{cases} y_1\left(t_0\right) = r_0;\ y_2\left(t_0\right) = \dot{r}_0 \\ y_3\left(t_0\right) = \theta_0;\ y_4\left(t_0\right) = \dot{\theta}_0 \\ y_5\left(t_0\right) = z_0;\ \ y_6\left(t_0\right) = \dot{z}_0 \end{cases} \tag{2.82}$$

By substituting Eqs. (2.76)-(2.81) in Table 2-1, we obtain a system of first order differential equations that are presented in Table 2-2. This set of equations can then be programmed using any numerical software program (such as Mathematica, Fortran, Matlab, Mathcad, or Maple). Its solution and physical interpretation will be explored in the following chapter.

Table 2-2 Set of first order differential equations.

Variable	Components of forces in three directions
$\dot{y}_1$	$= y_2$
$\dot{y}_2$	$= y_1 y_4^2 + \frac{1}{\left(\rho_p V_p + C_m \rho_f V_p\right)}\left\{3\pi\mu D f(u_r - y_2) + \mu\pi\frac{D^3}{8}(\nabla^2 \boldsymbol{u})_r + C_m \rho_f V_p\left(u_r\frac{\partial u_r}{\partial r} + \frac{1}{y_1}u_\theta\frac{\partial u_r}{\partial \theta} + u_z\frac{\partial u_r}{\partial z} - \frac{u_\theta^2}{y_1}\right)\right.$ $\left. + V_p\left(u_r\frac{\partial u_r}{\partial r} + \frac{1}{y_1}u_\theta\frac{\partial u_r}{\partial \theta} + u_z\frac{\partial u_r}{\partial z} - \frac{u_\theta^2}{y_1}\right) + 1.61 D^2\sqrt{\mu\rho_f}\left(\left(\frac{1}{y_1}\frac{\partial u_z}{\partial \theta} - \frac{\partial u_\theta}{\partial r}\right)^2 + \left(\frac{\partial u_r}{\partial z} - \frac{\partial u_z}{\partial r}\right)^2 + \left(\frac{1}{y_1}\frac{\partial (r u_\theta)}{\partial r} - \frac{1}{y_1}\frac{\partial u_r}{\partial \theta}\right)^2\right)^{-1/4}\right.$ $\left. \times\left[\frac{1}{y_1}\left(u_\theta - y_1 y_4\right)\left(\frac{\partial (r u_\theta)}{\partial r} - \frac{\partial u_r}{\partial \theta}\right) - \left(u_z - y_6\right)\left(\frac{\partial u_r}{\partial z} - \frac{\partial u_z}{\partial r}\right)\right]\right\}$
$\dot{y}_3$	$= y_4$

Table 2-2 Continued

Variable	Components of forces in three directions
$\dot{y}_4$	$= -\frac{2y_2y_4}{y_1} + \frac{1}{y_1\left(\rho_p V_p + C_m\rho_f V_p\right)}\left\{3\pi\mu Df(u_\theta - y_1y_4) + \mu\pi\frac{D^3}{8}(\nabla^2\boldsymbol{u})_\theta + C_m\rho_f V_p\left(u_r\frac{\partial u_\theta}{\partial r} + \frac{1}{y_1}u_\theta\frac{\partial u_\theta}{\partial\theta} + u_z\frac{\partial u_\theta}{\partial z} + \frac{u_\theta u_r}{y_1}\right)\right.$ $+1.61D^2\sqrt{\mu\rho_f}\left[\left(\frac{1}{y_1}\frac{\partial u_z}{\partial\theta} - \frac{\partial u_\theta}{\partial r}\right)^2 + \left(\frac{\partial u_r}{\partial z} - \frac{\partial u_z}{\partial r}\right)^2 + \left(\frac{1}{y_1}\frac{\partial(ru_\theta)}{\partial r} - \frac{1}{y_1}\frac{\partial u_r}{\partial\theta}\right)^2\right]^{-1/4}$ $\left.+\rho_f V_p\left(u_r\frac{\partial u_\theta}{\partial r} + \frac{1}{y_1}u_\theta\frac{\partial u_\theta}{\partial\theta} + u_z\frac{\partial u_\theta}{\partial z} + \frac{u_\theta u_r}{y_1}\right)\times\left[\left(u_z - y_6\right)\left(\frac{1}{y_1}\frac{\partial u_z}{\partial\theta} - \frac{\partial u_\theta}{\partial z}\right) - \frac{1}{y_1}\left(u_r - y_2\right)\left(\frac{\partial(ru_\theta)}{\partial r} - \frac{\partial u_r}{\partial\theta}\right)\right]\right\}$
$\dot{y}_5$	$= y_6$
$\dot{y}_6$	$= \frac{1}{\left(\rho_p V_p + C_m\rho_f V_p\right)}\left\{3\pi\mu Df(u_z - y_6) + \mu\pi\frac{D^3}{8}(\nabla^2\boldsymbol{u})_z + \rho_f V_p(1 + C_m)\left(u_r\frac{\partial u_z}{\partial r} + \frac{1}{y_1}u_\theta\frac{\partial u_z}{\partial\theta} + u_z\frac{\partial u_z}{\partial z}\right) + 1.61D^2\sqrt{\mu\rho_f}\right.$ $\left.\times\left[\left(\frac{1}{y_1}\frac{\partial u_z}{\partial\theta} - \frac{\partial u_\theta}{\partial r}\right)^2 + \left(\frac{\partial u_r}{\partial z} - \frac{\partial u_z}{\partial r}\right)^2 + \left(\frac{1}{y_1}\frac{\partial(ru_\theta)}{\partial r} - \frac{1}{y_1}\frac{\partial u_\theta}{\partial\theta}\right)^2\right]^{-1/4}\left[\left(u_r - y_2\right)\left(\frac{\partial u_r}{\partial z} - \frac{\partial u_z}{\partial r}\right) - \left(u_\theta - y_1y_4\right)\left(\frac{1}{y_1}\frac{\partial u_z}{\partial\theta} - \frac{\partial u_\theta}{\partial r}\right)\right]$

Chapter 3

Mean Flow Models for Primary Phase

3.1 Solid Rocket Motor

F.E.C. Culick first presented the steady-state flow solution for a solid rocket motor [38]. His model was obtained by assuming the flow to be inviscid, axisymmetric, incompressible, and steady. To incorporate viscosity, Majdalani and Akiki [39] presented a mean flow solution that mimics the bulk gas motion in a solid rocket engine of chamber length L and radius a. A sketch of the chamber is given in Figure 3-1 where $\bar{r}$ and $\bar{z}$ are used to denote the radial and axial coordinates. Downstream of the base, the flow is accelerated after expanding through a nozzle whose treatment is not required here. The sidewall injection velocity U_w is used to represent the solid fuel regression rate.

3.1.1 Equations

The bulk gas flow is considered to be non-reactive, and furthermore, the basic flow may be assumed to be (i) steady, (ii) incompressible, (iii) rotational, (iv)

axisymmetric, and (v) viscous. Based on these assumptions, the Navier-Stokes equations become

$$\frac{1}{\overline{r}}\frac{\partial\left(\overline{r}\overline{u}_{r}\right)}{\partial\overline{r}}+\frac{\partial\overline{u}_{z}}{\partial\overline{z}}=0 \tag{3.1}$$

$$\overline{u}_{r}\frac{\partial\overline{u}_{r}}{\partial\overline{r}}+\overline{u}_{z}\frac{\partial\overline{u}_{r}}{\partial\overline{z}}=-\frac{1}{\rho}\frac{\partial\overline{p}}{\partial\overline{r}}+\nu\left[\frac{\partial^{2}\overline{u}_{r}}{\partial\overline{z}^{2}}+\frac{\partial}{\partial\overline{r}}\left(\frac{1}{\overline{r}}\frac{\partial(\overline{r}\overline{u}_{r})}{\partial\overline{r}}\right)\right] \tag{3.2}$$

$$\overline{u}_{r}\frac{\partial\overline{u}_{z}}{\partial\overline{r}}+\overline{u}_{z}\frac{\partial\overline{u}_{z}}{\partial\overline{z}}=-\frac{1}{\rho}\frac{\partial\overline{p}}{\partial\overline{z}}+\nu\left[\frac{\partial^{2}\overline{u}_{z}}{\partial\overline{z}^{2}}+\frac{1}{\overline{r}}\frac{\partial}{\partial\overline{r}}\left(\overline{r}\frac{\partial\overline{u}_{z}}{\partial\overline{r}}\right)\right] \tag{3.3}$$

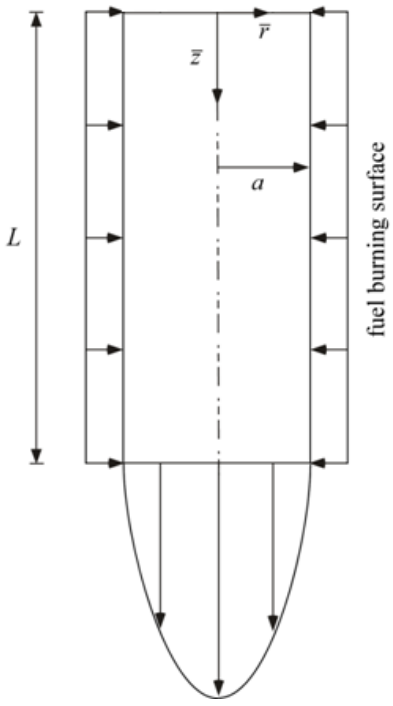

Figure 3-1 Sketch of a full-length solid rocket model depicting mass addition along the sidewall.

3.1.2 Boundary Conditions

The boundary conditions are due to symmetry and the no-slip requirement at the sidewall. Specifically, one can assume

(a) uniform injection along the cylindrical sidewall,

(b) no slip boundary condition at the sidewall,

(d) vanishing radial velocity along the centerline.

These particular conditions can be written as

$$\begin{cases} \overline{r} = a,\ 0 \le \overline{z} < L,\ \overline{u}_r = -U_w \ (\text{sidewall injection}) \\ \overline{r} = a,\ 0 \le \overline{z} < L,\ \overline{u}_z = 0 \ (\text{no slip at the wall}) \\ \overline{r} = 0,\ \forall \overline{z},\ \overline{u}_r = 0 \ (\text{no flow across centerline}) \end{cases} \tag{3.4}$$

3.1.3 Normalization

All of the variables and operators are normalized according to

$$z = \frac{\overline{z}}{a};\ r = \frac{\overline{r}}{a};\ \nabla = a\overline{\nabla};\ p = \frac{\overline{p}}{\rho U_w^2} \tag{3.5}$$

$$u_r = \frac{\overline{u}_r}{U_w};\ u_z = \frac{\overline{u}_z}{U_w} \tag{3.6}$$

Here $U_w = -\overline{u}_r(a, \overline{z})$ represents the uniform wall injection velocity at the sidewall. The corresponding boundary conditions reduce to

$$\begin{cases} u_r(1, z) = -1 \\ u_z(1, z) = 0 \\ u_r(0, z) = 0 \end{cases} \tag{3.7}$$

3.1.4 Viscous Rotational Solution

In the reduced Navier-Stokes equation, in which viscous effects and wall regression are incorporated, one can set $\alpha = 0$ to achieve the case corresponding to a stationary wall. One gets:

$$2\varepsilon\left(\theta\frac{\mathrm{d}^4F}{\mathrm{d}\theta^4}+2\frac{\mathrm{d}^3F}{\mathrm{d}\theta^3}\right)+F\frac{\mathrm{d}^3F}{\mathrm{d}\theta^3}-\frac{\mathrm{d}F}{\mathrm{d}\theta}\frac{\mathrm{d}^2F}{\mathrm{d}\theta^2}=0 \tag{3.8}$$

where

$$\psi=\frac{\bar{\psi}}{a^2U_w}=zF\,;\; u_r=-\frac{F}{r};\; u_z=\frac{z}{r}\frac{\mathrm{d}F}{\mathrm{d}r} \tag{3.9}$$

The corresponding boundary conditions are given :

$$\frac{\mathrm{d}F\left(\frac{1}{2}\pi\right)}{\mathrm{d}\theta}=0;\;\; F\left(\tfrac{1}{2}\pi\right)=1;\;\; F(0)=0\,;\;\lim_{\theta\to 0}\sqrt{\theta}\,\frac{\mathrm{d}^2F}{\mathrm{d}\theta^2}=0 \tag{3.10}$$

It is noted that $\varepsilon \equiv \nu/(a\ U_w)$ is the inverted Reynolds number based on the wall injection velocity. Equation (3.8) may be solved asymptotically by first setting $F=F_0+\varepsilon F_1+O(\varepsilon^2)$ and then inserting the expanded form back into Eq. (3.8). The analysis is explained in detail by Majdalani and Akiki [39]. Here, we present the final viscous solution that is used in the present work, specifically,

$$\begin{aligned}u_r=-\sqrt{\frac{\pi}{2\theta}}\Big[&\sin\theta+\varepsilon\Big(-3+\Big[3+S(\tfrac{1}{2}\pi)-S(\theta)\Big]\sin\theta\\&-\cos\theta\Big\{S_1(\theta)-3+\theta\Big[1+6\pi^{-1}+S(\tfrac{1}{2}\pi)-S(\theta)-2\pi^{-1}S_1(\tfrac{1}{2}\pi)\Big]\Big\}\Big)\Big]+O(\varepsilon^2)\end{aligned} \tag{3.11}$$

$$u_z = \pi\left(\frac{z}{a}\right)\Big[\cos\theta + \varepsilon\Big(-\theta + 2\Big[1 - 2\pi^{-1} + \pi^{-1}S_1(\tfrac{1}{2}\pi)\Big]\cos\theta + \Big\{S_1(\theta) - 3 + \theta\Big[1 + 6\pi^{-1} + S(\tfrac{1}{2}\pi) - S(\theta) - 2\pi^{-1}S_1(\tfrac{1}{2}\pi)\Big]\Big\}\sin\theta\Big)\Big] + O(\varepsilon^2) \quad (3.12)$$

where

$$\theta = \frac{\pi}{2}\left(\frac{r}{a}\right)^2 \quad (3.13)$$

$$S(\theta) = \theta + \sum_{k=1}^{\infty}\frac{2}{\pi^{2k}}\left(\sum_{n=1}^{\infty}\frac{1}{n^{2k}}\right)\frac{\left(1-2^{1-2k}\right)}{\left(2k+1\right)}\theta^{2k+1} \quad (3.14)$$

Table 3-1 Range of important parameters for simulated SRMs

Variable	Definition	Values	Reference value
U_w	Gas velocity at the burning surface	0.01-10 m/s	1 m/s
a	Combustion chamber radius	0.025-3 m	0.1 m
L/a	Length of combustion chamber	1-50	20
$\varepsilon \equiv \upsilon / (aU_w)$	Inverted Reynolds number	0.01-0.0001	0.001
ρ_p / ρ_f	Relative density	100-1000	500
μ	Chamber gas dynamic velocity	3×10^{-5} – 3×10^{-4} Ns/m^2	3×10^{-5} Ns/m^2
D	Diameter of particle	10-500 μm	100 μm

$$S_1(\theta) = \tfrac{1}{2}\theta^2 + \sum_{k=1}^{\infty}\left(\sum_{n=1}^{\infty} n^{-2k}\right)\frac{\left(1-2^{1-2k}\right)}{\left(k+1\right)\pi^{2k}}\theta^{2k+2} \tag{3.15}$$

3.1.5 Typical Parameters for Solid Rocket Motors

Important parameters in SRMs are supplied in Table 3.1 over the entire range of interest For our study of particle trajectories, the reference values given in the last column have been used.

3.2 Bidirectional Vortex Engine

Majdalani [40] presented a uniformly valid solution for the chamber of a bidirectional vortex engine. Their model provides the gas motion in a cylindrical chamber of length *L* and radius *a*, with a closed headwall (defined at $\overline{z} = 0$). Here spatial coordinates $\overline{r}$ and $\overline{z}$ are normalized by the chamber radius *a*. The ratio of open flow in the exit plane is defined as $\beta = b/a$, and the chamber aspect ratio is defined as $l = L/a$ (see Figure 3-2). The oxidizer gas is injected at high velocity at the base of the cylinder to induce a swirling annular stream that clings to the wall and traverses the length of the chamber in what is known as the outer vortex region. At the headwall, the flow turns and forms the core vortex that exits at the base of the chamber.

3.2.1 Normalization

It is helpful in asymptotic treatments to normalize all key equations. The choices for normalization are given in Eqs. (3.16)–(3.18), where $\overline{Q}_i$ and $\overline{Q}_o$ represent the

volumetric flow rates at the chamber inlet and outlet, respectively. Here *U* represents the average fluid injection velocity. The normalization of all variables follows from :

$$z = \frac{\overline{z}}{a}; r = \frac{\overline{r}}{a}; \nabla = a\overline{\nabla} \tag{3.16}$$

$$u_r = \frac{\overline{u}_r}{U}; \quad u_\theta = \frac{\overline{u}_\theta}{U}; \quad u_z = \frac{\overline{u}_z}{U} \tag{3.17}$$

$$p = \frac{\overline{p}}{\rho U^2}; \quad Q_i = \frac{\overline{Q}_i}{Ua^2}; \quad Q_o = \frac{\overline{Q}_o}{Ua^2} \tag{3.18}$$

3.2.2 Equations

After entering the chamber, fluid particles follow a helical trajectory by spirally around the entire length of the chamber twice before exiting at the base. Here too the basic flow can be assumed to be (i) steady, (ii) incompressible, (iii) viscous, and (iv) axisymmetric. The swirl velocity is assumed to be axially independent. Upon application

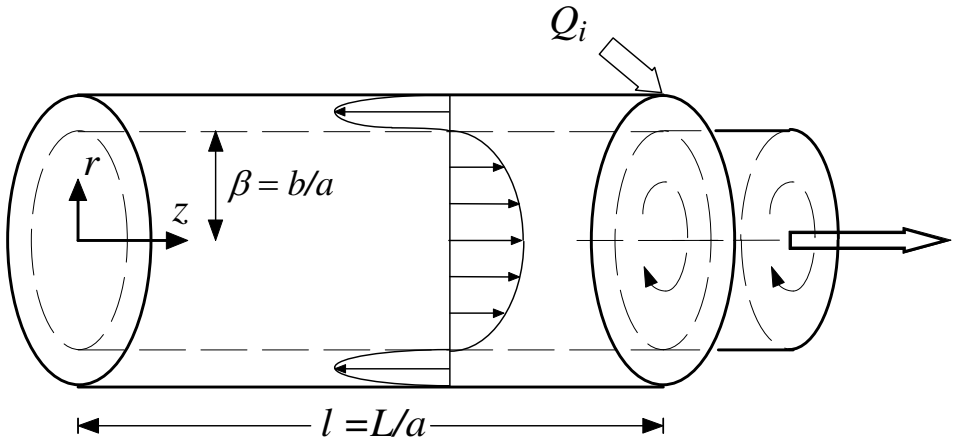

Figure 3-2 Bidirectional vortex engine diagram [40].

of the new non-dimensionalized variables, the governing equations can be expressed in a more suitable form and the Navier-Stokes equations become:

$$\frac{1}{r}\frac{\partial\left(ru_r\right)}{\partial r}+\frac{\partial u_z}{\partial z}=0 \tag{3.19}$$

$$u_r\frac{\partial u_r}{\partial r}+u_z\frac{\partial u_r}{\partial z}-\frac{u_\theta^{\,2}}{r}=-\frac{\partial p}{\partial r} \tag{3.20}$$

$$u_r\frac{\partial u_\theta}{\partial r}+\frac{u_\theta u_r}{r}=0 \tag{3.21}$$

$$u_r\frac{\partial u_z}{\partial r}+u_z\frac{\partial u_z}{\partial z}=-\frac{\partial p}{\partial z} \tag{3.22}$$

3.2.3 Boundary Conditions

The first set of boundary conditions are due to symmetry and the infinite impedance of the walls. The second set is due to the inlet configuration and bulk mass conservation. Physically, these consist of the following:

(a) a fully tangential inflow,

(b) a zero axial flow at the headwall,

(c) symmetry about the centerline,

(d) a zero radial flow at the sidewalls, and

(e) an inflow that matches the outflow

These can be written as

$$\begin{cases} u_\theta\left(1\right)\Big|_l = 1; \\ u_z\left(r,0\right) = 0; \\ u_r\left(0,z\right) = 0 \\ u_r\left(1,z\right) = 0; \\ Q_o = \int_0^{2\pi}\int_0^{\beta} \boldsymbol{u}\left(r,l\right)\cdot \boldsymbol{n}\, r\ \mathrm{d}r\ \mathrm{d}\theta = Q_i \end{cases} \tag{3.23}$$

According to Hoekstra, Derksen and Van den Akker [41], the relation between the normalized volumetric flow rate, Q_i, and the swirl number, *S,* used in the literature may be written as

$$S \equiv \frac{\pi ab}{A_i} = \frac{\pi\beta a^2}{A_i} = \frac{\pi\beta}{Q_i} \tag{3.24}$$

Accordingly, the geometric inflow parameter may be defined as

$$\kappa \equiv \frac{Q_i}{2\pi l} = \frac{A_i}{2\pi a l} = \frac{A_i}{2\sqrt{2}Sl} \tag{3.25}$$

3.2.4 Solution

Using matched asymptotic expansions (MAE), a uniformly valid analysis is obtained by Majdalani [40], namely,

$$u_r\left(r\right) = -\frac{\kappa}{r}\sin\left(\pi r^2\right)\left\{1-\exp\left[-\sqrt{V}\left(1-r\right)\right]\right\} \tag{3.26}$$

$$u_\theta\left(r\right) = \frac{1}{r}\left[1-\exp\left(-\tfrac{V}{4}r^2\right)-\exp\left[-\sqrt{V}\left(1-r\right)\right]\right] \tag{3.27}$$

$$u_z\left(r,z\right) = 2\pi\kappa z\cos\left(\pi r^2\right)\left\{1-\exp\left[-\sqrt{V}\left(1-r\right)\right]\right\} \tag{3.28}$$

The above represents the uniformly valid asymptotic solution that is used in the present work, where the vortex Reynolds number is given by

$$V = \frac{Re}{S}\frac{\pi a\beta}{L} = 2\pi\kappa Re \tag{3.29}$$

3.2.5 Axial, Radial and Azimuthal Velocity Profiles

Understanding the velocity profiles is important when analyzing the particle

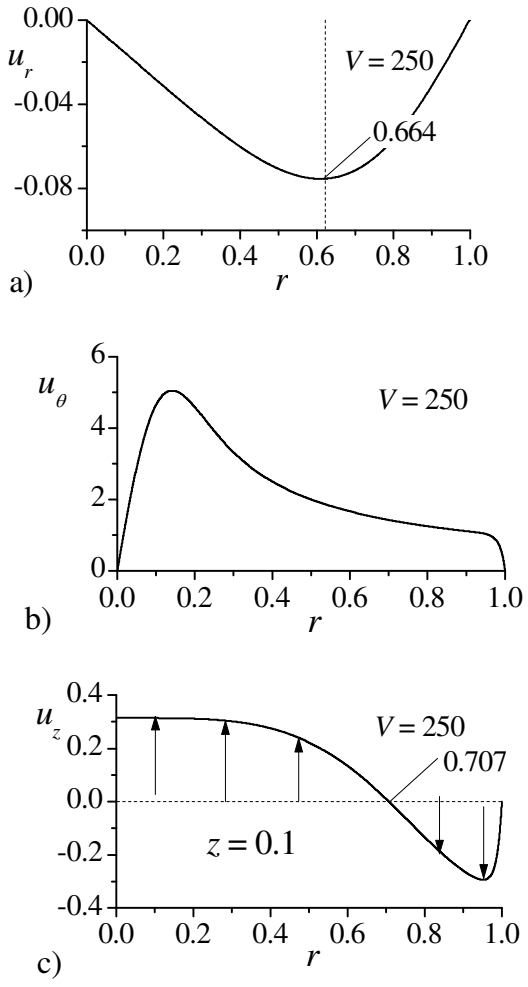

Figure 3-3 Velocity plot illustrating: a) axial velocity, b) azimuthal velocity, and c) radial velocity profiles in a simulated bidirectional vortex engine.

trajectories in the bidirectional vortex engine. The radial velocity is zero along the sidewall as there is no gas injection normal to the wall. The radial velocity peaks in the vicinity of the mantle as shown in part (a) of Figure 3-3. The radial velocity remains independent of z and therefore invariant at any axial location. The azimuthal velocity, u_θ , as shown in part (b) of Figure 3-3, depends on the radial coordinate only. Based on Eq. (3.27), it peaks near the axis, within the inner vortex, and decreases near the wall, within the outer vortex. The axial velocity distribution, captured by Eq. (3.28), is a linear function of the axial distance from the chamber headwall. Note that linearly u_z decreases as the fluid approaches z=0. Here, the radial distribution of u_r is shown at a chamber length of 0.1 in part (c) of Figure 3-3. Clearly, the axial profile shows that the flow changes directions at the radial point r=0.707.

3.2.6 Typical Parameters for Bidirectional Vortex Engine

The range of parameters used in the BDVE over the entire range of interest is given in Table 3-2. For our study of particle trajectories, the reference values tabulated in the right-most column are used.

Table 3-2 Range of important parameters for the bidirectional vortex engine simulation

Variable	Definition	Values	Reference value
U	Oxidizer injection velocity	10-100 m/s	50 m/s
a	Radius of combustion chamber	0.001-0.1 m	0.1 m
L/a	Length of combustion chamber	1-10	5
κ	Geometric inlet parameter	0.01-0. 1	0.05
V	Vortex Reynolds number	100-500	250
ρ_p / ρ_f	Relative density	10-500	100
D	Diameter of particle	1-50 μm	25 μm

Chapter 4

Solid Rocket Motor Simulation Results

4.1 Reynolds Number and Magnitude Analysis of Forces

In our study we use a Lagrangian approach where inert aluminum particles ranging in diameter from 10 to 500 μm and from 10 to 1000 in relative density, ρ_p / ρ_f , are injected at different axial positions of the propellant burning surface and then tracked along the length of the chamber. The detailed analysis of forces that act on a particle is given in Chapter 2. In deriving the drag force, we take the relative Reynolds number to be less than unity, which is consistent with the Stokes flow assumption. Generally, the relative Reynolds number in two phase flows will be small if a particle moves in the direction of the flow, as it turns out to be the case in solid rocket motors. In addition to particle velocity and direction in the flowfield, the particle size and density ratio are important parameters affecting the relative Reynolds number. The relative Reynolds numbers acting on a 100 μm particle with different density ratios and on a particle with

different radii are shown in parts (a) and (b) of Figure 4.1, respectively. We can see in part (a) that the relative Reynolds number is very low for low density ratios. However, a significant increase in the Reynolds number can be seen when the density ratio is

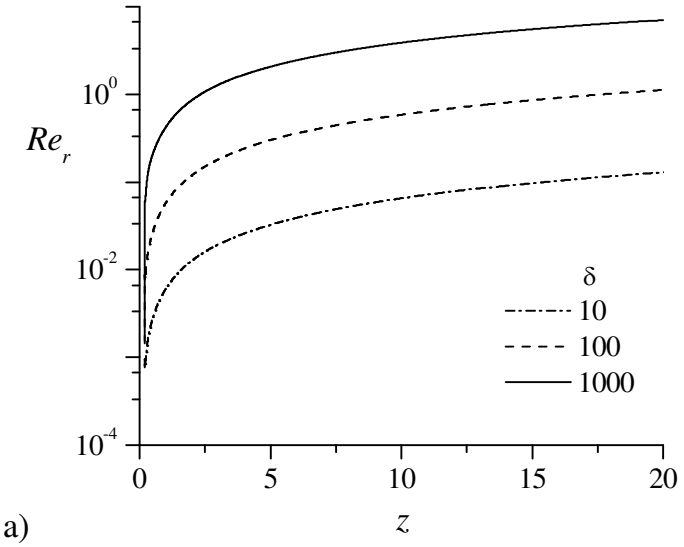

a)

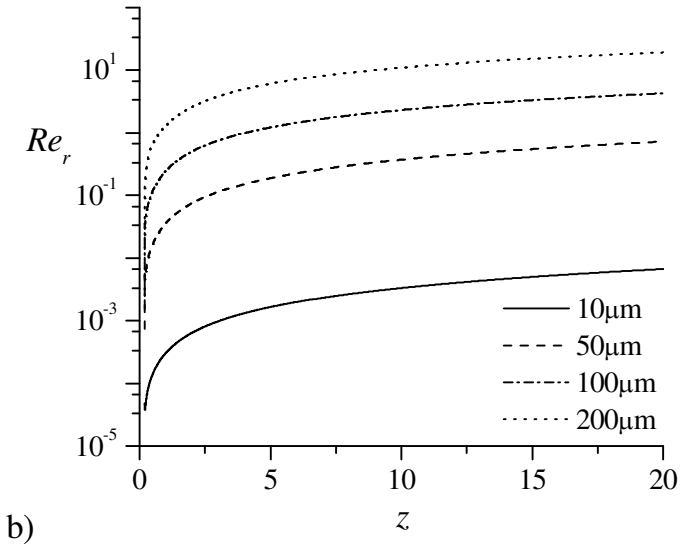

b)

Figure 4-1 Variation of the relative Reynolds number along the non-dimensional length of the simulated SRM chamber for: a) 100 μm particles with varying density ratios, and b) particles with different radii at fixed δ = 500.

increased to 1000. Because the density of an aluminum particle is constant, the relative density can only be decreased by increasing the density of the gas phase, which in turn increases the Reynolds number (refer to Eq. 3.30). Part (b) of Figure 4.1 shows that the relative Reynolds number increases as it should, when the size of the particle increases.

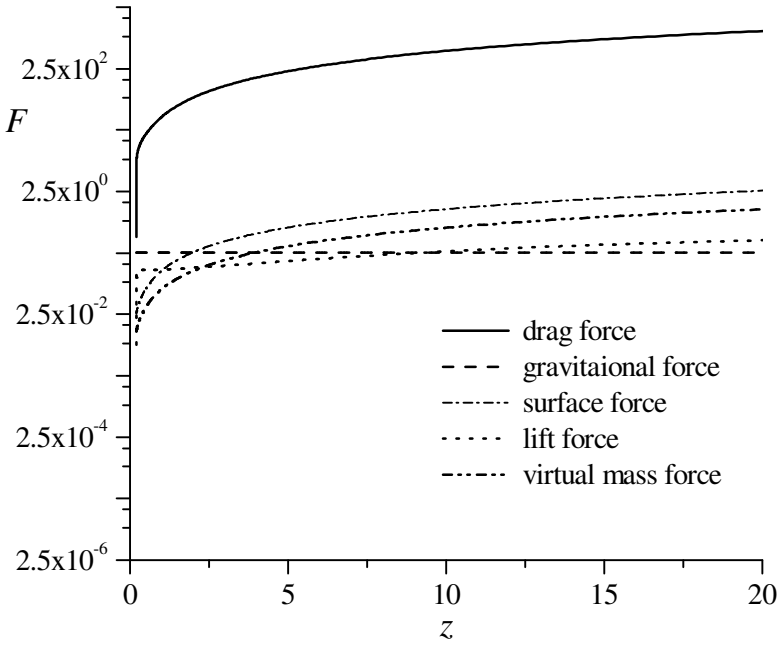

Figure 4-2 Comparison of forces acting on a 100 μm particle in a simulated SRM taken along the non-dimensional length of the chamber axis z for a sidewall injection velocity of U_w = 10 m/s and δ = 500.

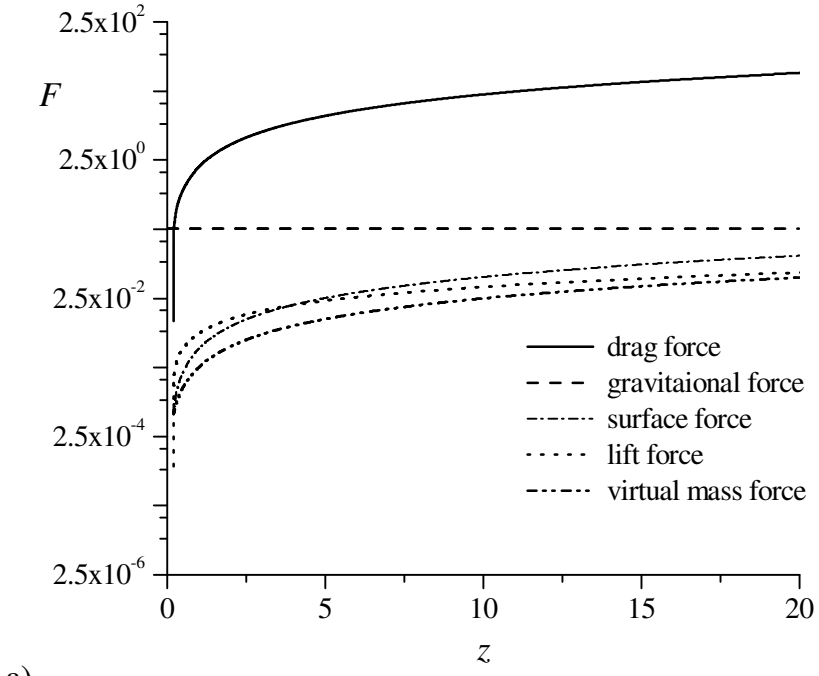

a)

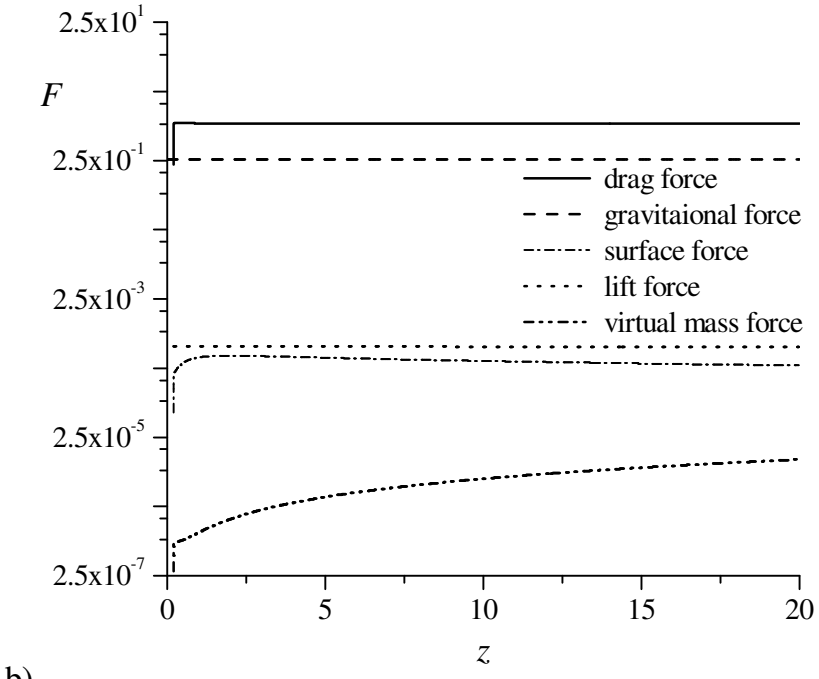

b)

Figure 4-3 Comparison of forces acting on a 100 µm particle in a simulated solid rocket motor along the non-dimensional length of the combustion chamber axis z for sidewall injection velocities of: a) U_w = 1 m/s and b) U_w = 0.1 m/s at fixed δ = 500.

In most of the studies conducted on nozzle erosion, all but the drag force are neglected in order to simplify an otherwise complex multiphase flow problem, so to validate and examine the magnitude of forces acting on particles, a magnitude analysis of forces is performed by predicting the forces experienced by a 100 µm particle injected at the headwall as it traverses the length of the combustion chamber (shown in Figure 4-2 and Figure 4-3) for different sidewall injection velocities. In our study the forces are non-dimensionalized by $\rho_f \, U_w^2 \, D^2$, where reference values of ρ_f , U_w and D are taken from Table 3-1.

Inspection of Figure 4-2 and Figure 4-3 reveals that the virtual, lift and gravity are

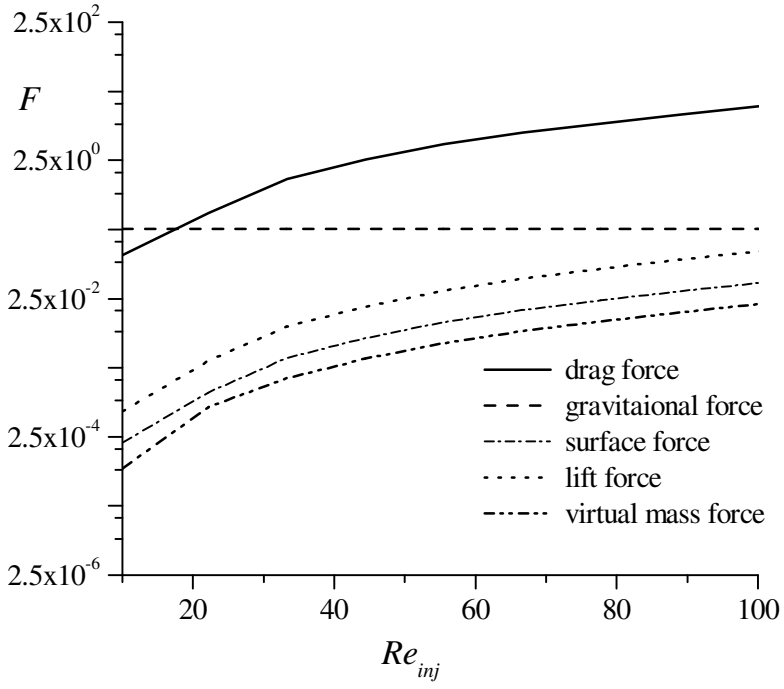

Figure 4-4 Comparison of forces acting on a 100 µm particle in a simulated solid rocket motor at non dimensional axial distance of z=10 and an injection Reynolds number ranging from 10 to100.

the least dominant forces for sidewall injection velocities of 10 and 1 m/s. At such high velocities, drag and surface forces are the most appreciable. However, for a sidewall injection velocity of 0.1 m/s (low end), the role of the surface force is taken by the gravitational force. Thus, for low sidewall injection velocities, the weight of the particle must be included in flow simulation.

4.1.1 Effect of Injection Reynolds Number Re_{inj} on Forces

The effect of injection velocity on various forces is discussed in the previous sections. To capture the effect of injection velocity on various forces, a magnitude analysis is carried out at a chamber length of 10, which is halfway along the combustion chamber. This is accomplished by varying the injection Reynolds number, $Re_{inj}=(aU_w)/\nu$, from 10 to 100 as shown in Figure 4-4. From Figure 4-4 it can be seen that for $Re_{inj} <$ 17.7 the gravitational force is the largest; however, for $Re_{inj}>17.7$, the drag force dominates and the magnitude of forces increase as the injection Reynolds number is increased. Thus at large injection velocities, all the forces considered here may be included in our analysis but their effects will be smaller than that of the drag force.

4.1.2 Effect of Particle Size and Sidewall Injection Velocity at Burning Surface

The steady-state flow solution in solid rocket motors is dependent on the sidewall injection velocity, U_w. In general, the sidewall injection velocity values range from 0.01 to 10 m/s under normal operating conditions, with 1 being the most common. To examine the effect of the sidewall injection velocity, particle trajectories and radial distributions of

particles at the exit of the combustion chamber are shown in Figure 4-5 for a velocity of 1 m/s and, in Figure 4-6, for a sidewall injection velocity of 0.01 m/s. The particle movement in the radial direction is reduced in Figure 4-6 because of the lower radial velocity. Comparison of Figure 4-5 and Figure 4-6 also shows that particles with radii between 10 and 100 μm exit the combustion chamber at a radial distance varying from

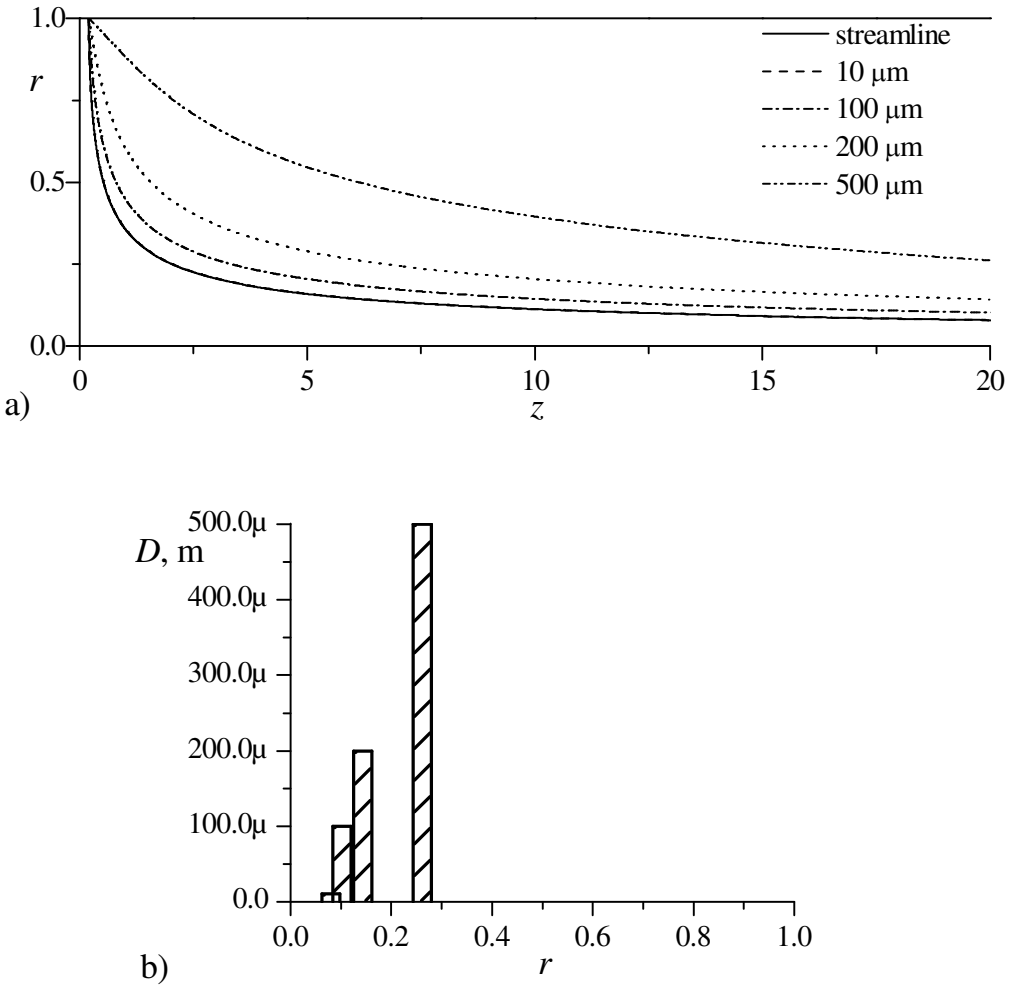

Figure 4-5 Part (a) depicts the trajectories of particles with different sizes that enter the chamber at a non-dimensional axial distance of z = 0.1 (here both drag and weight are considered). In part (b), the radial distribution of particles is shown at a downstream position corresponding to a non-dimensional axial distance of z = 20 and a fixed sidewall velocity of U_w = 1 m/s.

0.1 to 0.2 in both cases.

It should be noted that everywhere the particles with larger diameters tend to move closer to the wall. Furthermore, the resulting particle concentration will shift towards the wall as U_w is reduced. This can partially explain the cause of nozzle

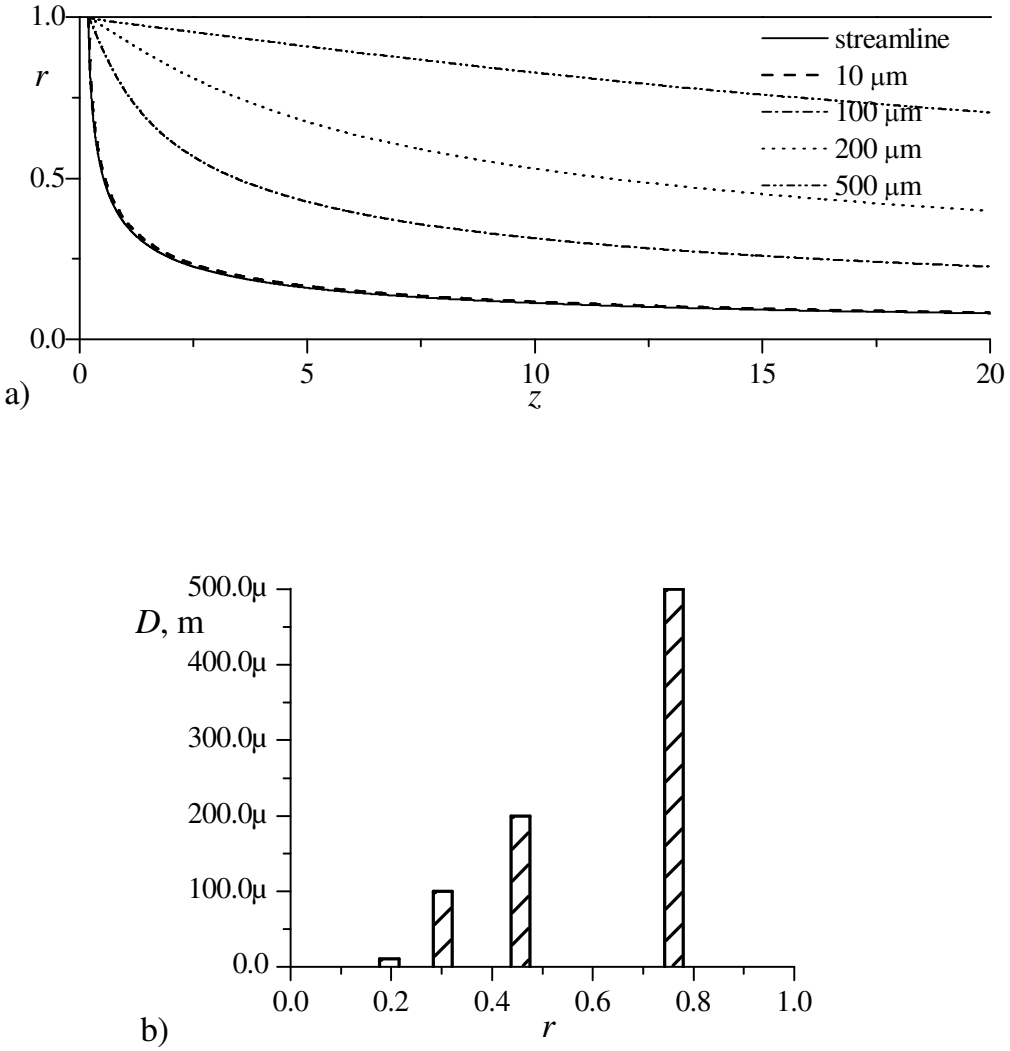

Figure 4-6 Part (a) depicts the trajectories of particles with different sizes that enter the chamber at a non-dimensional axial distance of z = 0.1 (here both drag and weight are considered). In part (b), the radial distribution of particles is shown at a downstream position corresponding to a non-dimensional axial distance of z = 20 and a fixed sidewall velocity of U_w = 0.01 m/s.

impingement and aluminum slag deposition in solid rocket motors.

4.1.3 Effect of Density Ratio.

The particle-to-gas density ratio in SRMs is another important parameter affecting particle trajectories. The most common ratios in SRMs range from 100 to 1000. Hence,

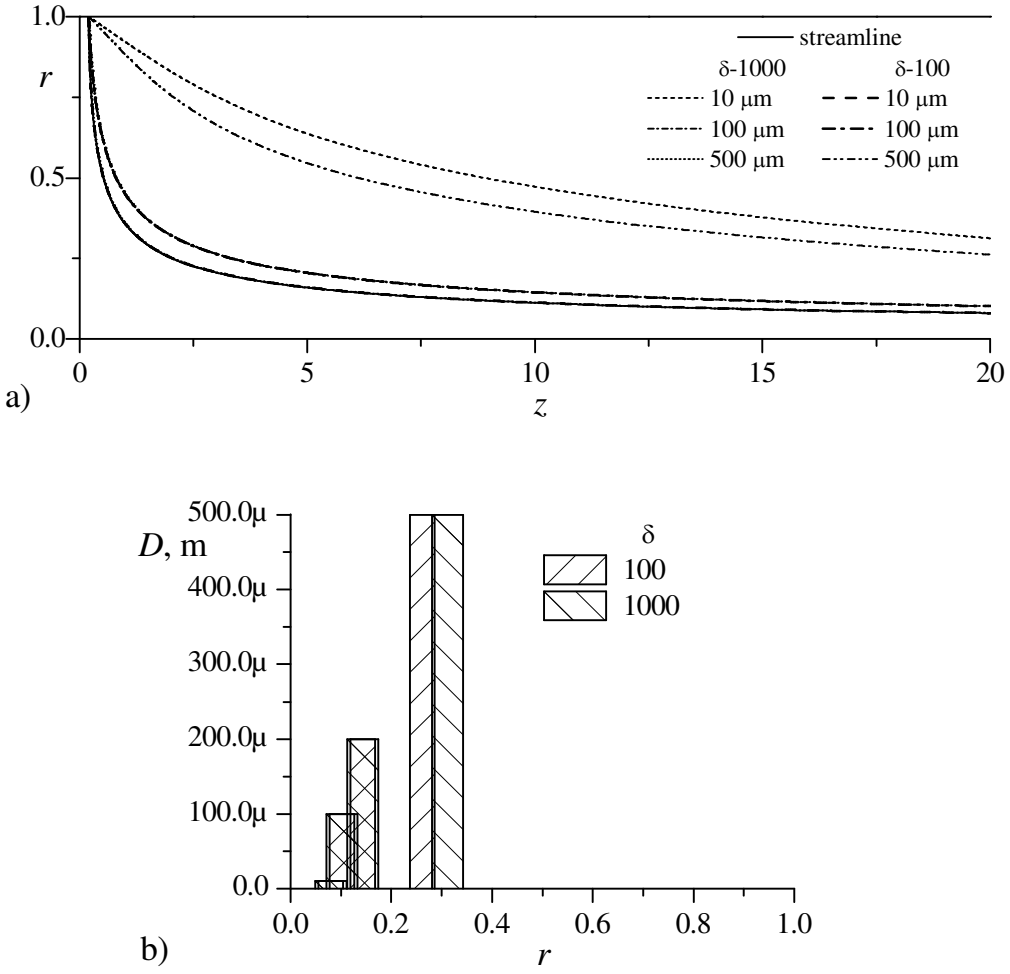

Figure 4-7 Part (a) depicts the trajectories of particles with different sizes that enter the chamber at a position corresponding to a non-dimensional axial distance of z =0.1 (here both drag and weight are considered). In part (b), the radial distribution of particles is shown at a downstream position corresponding to a non-dimensional axial distance of z = 20 and a fixed sidewall velocity of U_w = 0.01 m/s using density ratios of 100 and 1000.

simulations are run for these conditions. Part (a) in Figure 4-7 illustrates the trajectories of different size particles given these ratios. Most of the particles with different density ratios follow the same trajectories except for the 500 μm particles. The larger particles turn quickly towards the nozzle because, as their relative density increases, their inertia increases as well. This causes them to move away from their corresponding fluid flow streamlines. It can therefore be seen that the density ratio plays an important role for large agglomerates, but does not significantly affect the trajectories of smaller, single particles. The radial distribution of different size particles is shown in part (b) of Figure 4.6. Here, only a very small difference in distribution for different density ratios is observed. Therefore, it can be concluded that the density ratio has a weaker influence on particle trajectory for small-size particles with radii between 10 and 100 μm but can play an important role when considering particles with radii greater than 100 μm.

Chapter 5

Bidirectional Vortex Engine Simulation Results

Tracking particle motion in a bidirectional vortex (BV) engine is important to develop an understanding of the entrainment characteristics of fuel droplets injected into the chamber often near the headwall section, radially or axially. To this end, several particles with different radii and relative densities will be injected near the headend of the chamber to the extent that their trajectories may be examined. The various forces acting on the particles are presented in Chapter 2. In what follows, the significance of each force in determining the trajectory of a particle in a bidirectional vortex engine will be presented and discussed.

5.1 Reynolds Number and Magnitude Analysis of Forces

To start, a 25 μm particle is injected at a radial position of $r = 0.1$ with a relative

density of , ρ_p / ρ_f = 100. The forces are non-dimensionalized by $\rho_f U^2 D^2$ where reference values of ρ_f, U, and D are taken from Table 3.2. From Figure 5-1, it is clear that the drag force is dominant in determining the trajectory of a particle, whereas the lift, surface, and virtual mass forces are less important. In this case, gravity appears to be the least significant. Since the forces other than drag are too small to affect particle trajectory, we will only consider drag in subsequent analysis.

To better characterize the Reynolds number effect, the relative Reynolds number is plotted versus axial location for varying density ratios and particle sizes, as shown in Figure 5-2. It can be seen that the relative Reynolds number decreases as the particle size

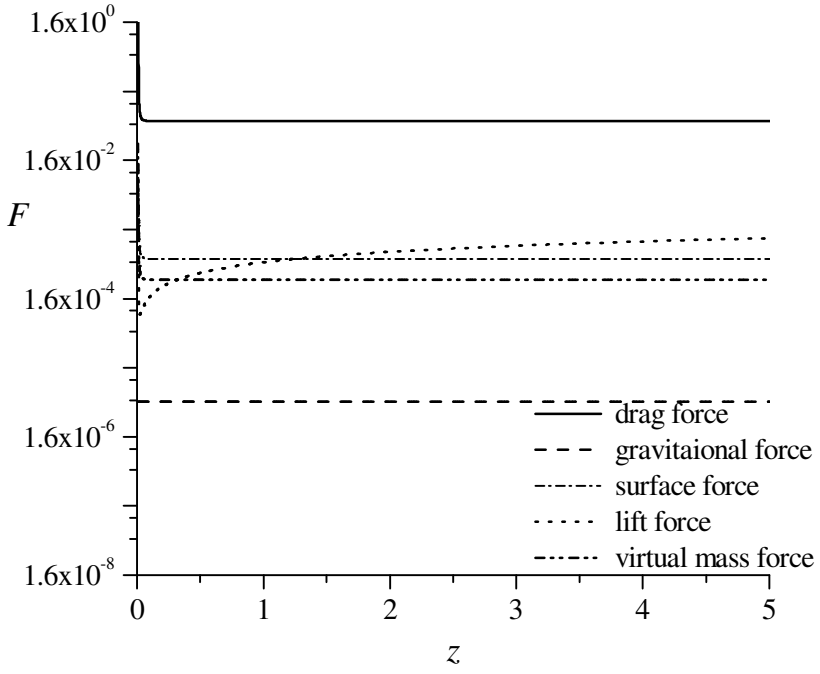

Figure 5-1 Comparison of forces acting on a 25 µm particle in a simulated bidirectional vortex engine taken along the non-dimensional length of the chamber axis z at fixed δ = 100.

decreases, as shown in Figure 5-2a, which is consistent with Eq. (2.22). The converse is of course true as the relative Reynolds number increases with successive increases in observed from Figure 5-2 concerning the Stokes regime. We recall that in Chapter 2, the

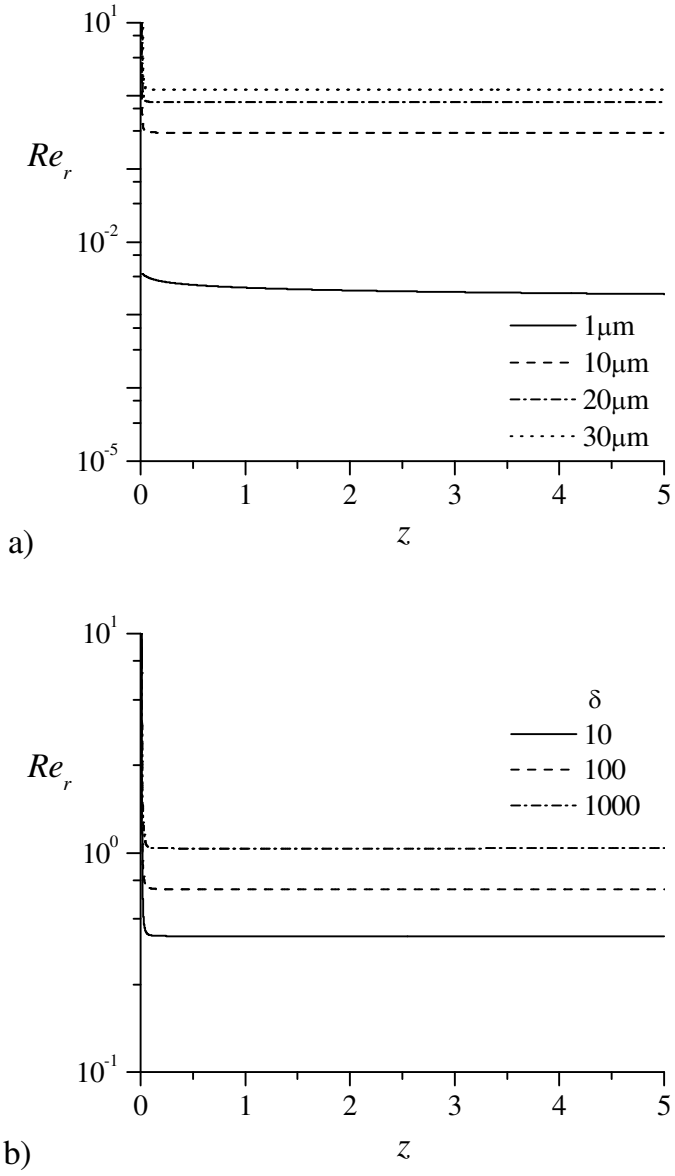

Figure 5-2 Variation of the relative Reynolds number along the non-dimensional length of the simulated bidirectional vortex engine chamber for: a) particles with different radii at fixed δ = 100, and b) 25 μm particles with varying density ratios.

particle density, as shown in Figure 5-2b. Thus, particles with larger densities give rise to larger Reynolds numbers. Another important result can be drag force on a spherical particle is derived assuming creeping flow (Re < 1) by neglecting the inertial terms in the Navier-Stokes equation. Figure 5-2 confirms that the relative Reynolds number in a bidirectional vortex engine is generally less than unity, thus justifying the Stokes flow approximation.

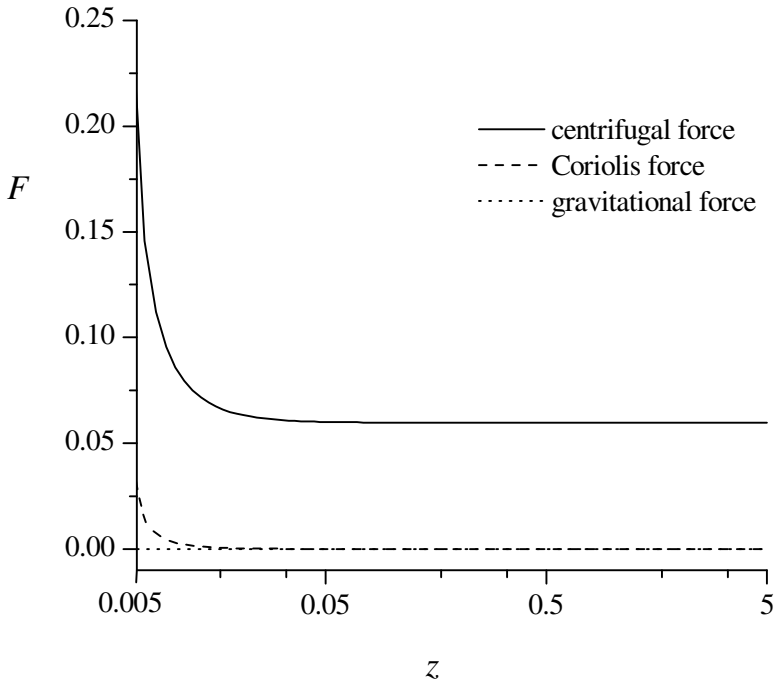

Figure 5-3 Comparison of centrifugal, Coriolis and gravitational forces acting on a 25 μm particle in a bidirectional vortex engine along the non-dimensional length of the combustion chamber axis *z*.

5.2 Effect of Particle Size

A particle trajectory is a function of different parameters such as size, density ratio, geometric inlet parameter, and particle axial velocity. The effects of these variables are studied parametrically. Particles with radii of 1 µm, 25 µm and 50 µm are injected at different dimensionless radial positions of 0.1, 0.5, and 0.9. Their respective trajectories are plotted in Figure 5-4. A graphic inspection reveals that small particles with radii of 1 µm and 25 µm, when injected near the centerline, initially move away from the core because of the centrifugal force and then get entrained in the inner vortex. When particles are injected near the wall, they move towards the wall. Unlike the smaller particles, from Figure 5-4 we see that larger particles, when injected near the centerline, move away

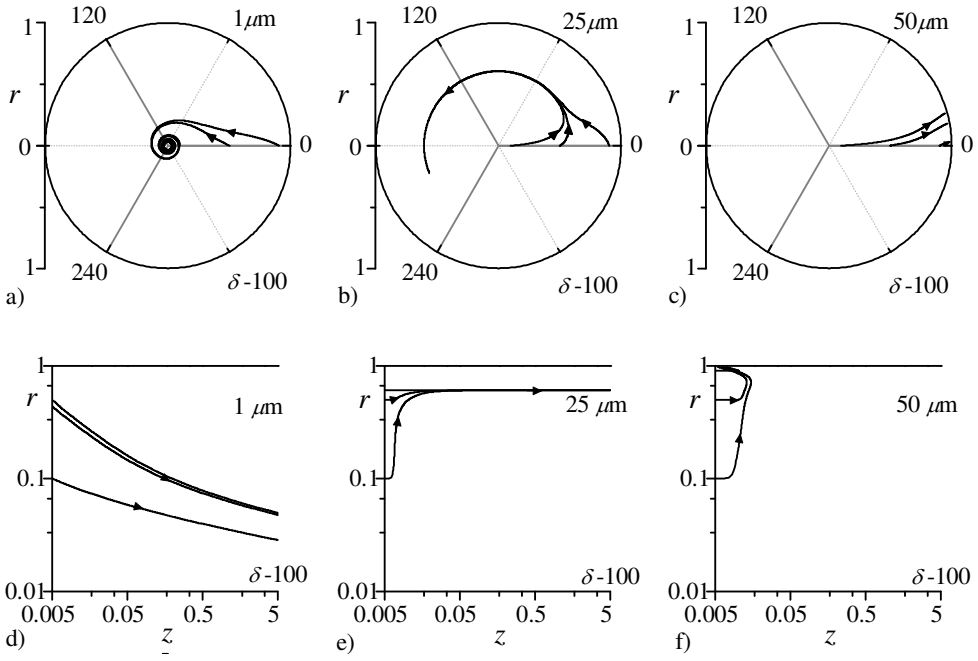

Figure 5-4 Trajectories of different size particles of same density originating from equidistant points taken along the radius of the combustion chamber.

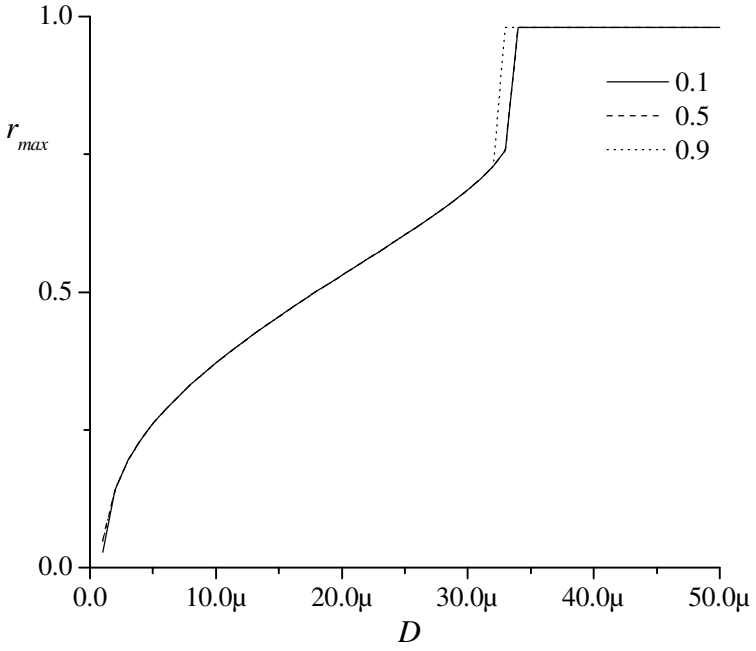

a)

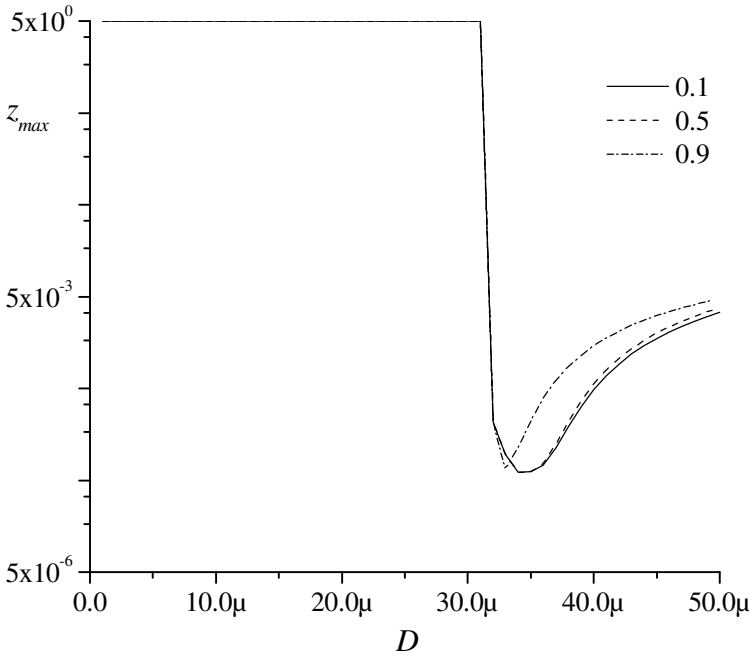

b)

Figure 5-5 Maximum radial and axial distance travelled by particles in a BDVE.

from inner vortex because of the proportionately high centrifugal force acting on them and, as a result, migrate towards the sidewall.

The movement of heavier particles towards the wall is caused by the strong centrifugal force, which can be seen in Figure 5-3, where a comparison of the centrifugal Coriolis and gravitational forces is given. This is accomplished by injecting a 25 μm particle axially at dimensionless radial position of 0.1 and chamber length of z=0.001. It can be seen from Figure 5-3 that the influence of centrifugal forces are higher than Coriolis forces on particles. As expected, the magnitude of both forces decreases as the particle moves along the combustion chamber. For example, the trajectory of a particle injected at a radial position of 0.1 in Figure 5-4b follows that of a ball traveling along a curved path on a rotating disc and subject to both Coriolis and centrifugal forces [28]. Part (f) of Figure 5-4 reveals an interesting phenomenon. The 50 μm particles, because of the higher centrifugal force acting on them, initially move towards the wall while migrating in the positive z-direction. However after crossing the BV mantle into the outer vortex, they reverse axial direction and drift towards the headwall.

It should be borne in mind that Figure 5-4 is only qualitative to the extent that a conclusion cannot be made about the limiting size of a particle that may be impacting the wall. To better understand the particle behavior in the BDVE, the loci of the maximum radial and axial distances travelled by particles are calculated and provided in Figure 5-5. Here, particles are injected at dimensionless radial positions of 0.1, 0.5 and 0.9 with diameters ranging from 1 to 50 μm near the headend at z=0.001. When a 1 μm particle is injected at a dimensionless radial position 0.1, we see in part (a) of Figure 5-5 that the

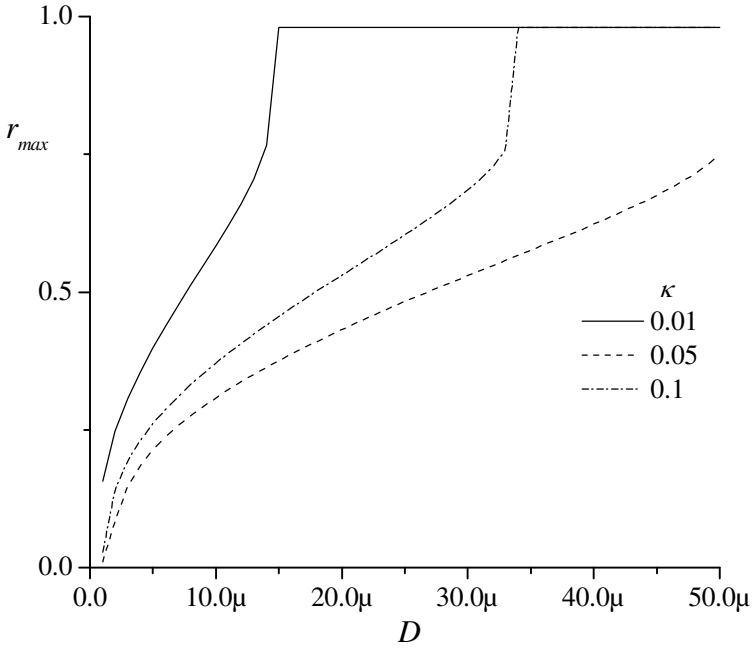

a)

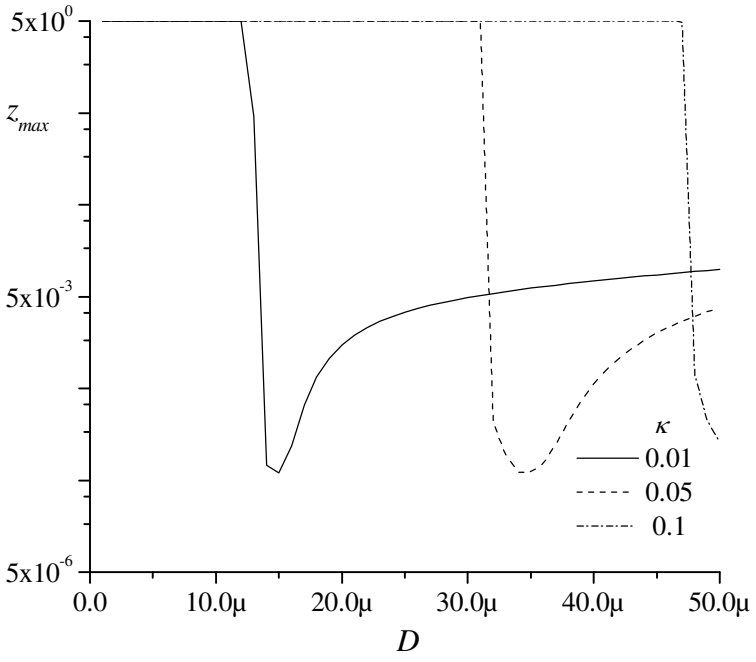

b)

Figure 5-6 Trajectories of different size particles of identical density with varying geometric inlet parameter. All particles are injected at a radial distance of r = 0.1.

particle will not reach the wall but instead will exit the chamber. However, when a 50 μm particle is injected at the same radial position of 0.1, it will reach the wall at approximately z = 0.00378 while moving axially. Figure 5-5 gives an overall idea about the particle trajectory history in the BDVE when injected at different radial positions. This can be useful in designing fuel injectors with the objective of confining the combusting fuel droplets to the inner vortex region.

5.3 Geometric Inlet Parameter (κ)

One of the most important parameters that can significantly change the trajectories of particles is the geometric inflow parameter, κ as previously described in Eq. (3.25). This parameter is important because it combines the volumetric flow rate of oxidizer injected tangentially into the combustion chamber and the swirl number. To capture the effect of κ, particle trajectories are calculated by varying the parameter from 0.01 to 0.1. It is noted here that lower values of κ correspond to higher tangential injection velocities at entry.

In part (a) of Figure 5-6, the maximum radial distance travelled by particles injected at a radial distance of 0.1 is shown for the purpose of illustrating particle movement along the combustion chamber. Similarly, part (b) captures the maximum axial distance travelled by the same particles. Particles injected at a radial distance of 0.9 from the center are shown in Figure 5-7. From Figure 5-6 and Figure 5-7, it is clear that for κ = 0.1, particles with radii less than 50 μm injected at a radius of 0.1 and 0.9 remain

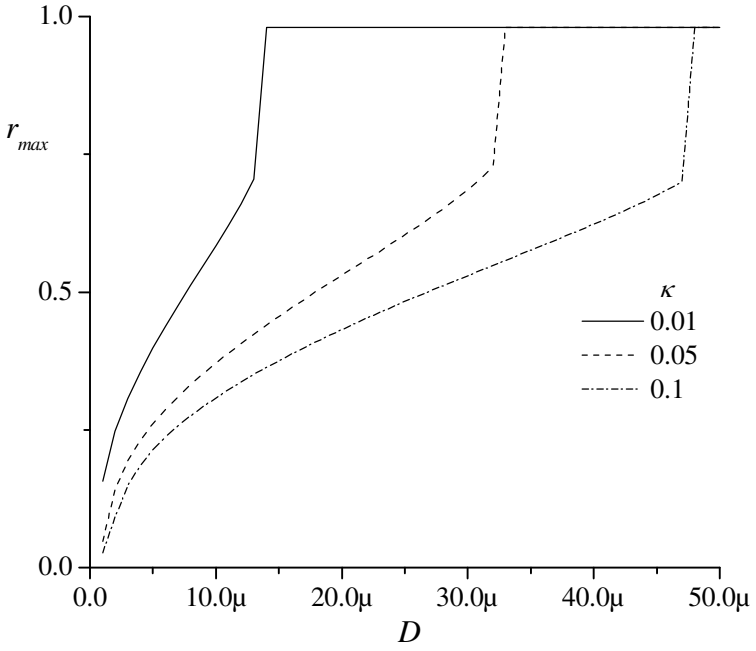

a)

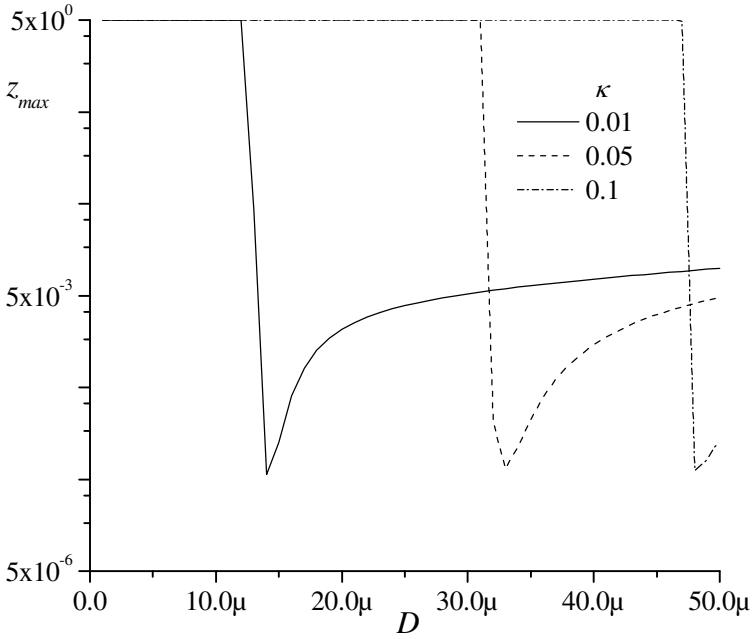

b)

Figure 5-7 Trajectories of different size particles of identical density with varying geometric inlet parameter. All particles are injected at a radial distance of r = 0.9.

confined to the inner vortex tube before exiting the combustion chamber. When $\kappa = 0.05$, particles with radii greater than 34 μm impact the chamber wall, thus creating hot spots. As the geometric inlet parameter is decreased to $\kappa = 0.01$, particles with smaller radii move away from the inner vortex and impact the wall.

The results presented in Figure 5-6 and Figure 5-7 suggest that the larger particles entering the chamber move into the outer vortex and contact the chamber wall instead of remaining confined to the inner vortex. This behavior can be explained as follows. Because the swirl intensity of the flowfield in the bidirectional vortex engine is inversely proportional to κ, decreasing the value of κ is tantamount to a scenario in which the swirl velocity is increased. Evidently, higher tangential velocities throughout the flowfield lead to larger centrifugal forces, and these, in turn, act on the particles in the outward radial direction. Given sufficiently small values of κ, particles are dragged toward the sidewall irrespective of their radius. One can therefore conclude that particle trajectories strongly depend on the inlet flow parameter κ.

5.4 Effect of Density Ratio (δ)

To study the effect of the density ratio on particle trajectory, particles with different radii are injected at a radial distance of $r = 0.1$ near the headwall center, with varying density ratios (see Figure 5-8).

From Figure 5-8, it can be seen that for $\delta = 10$, particles with radii less than 50 μm injected at a radius of 0.1 remain confined to the inner vortex tube before exiting the combustion chamber and from part (a) in Figure 5-8, it can be seen that when the density

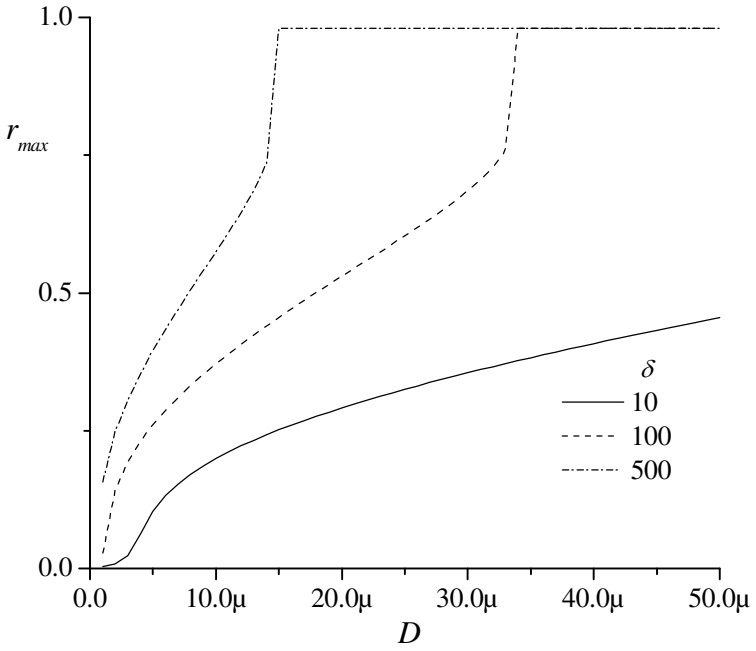

a)

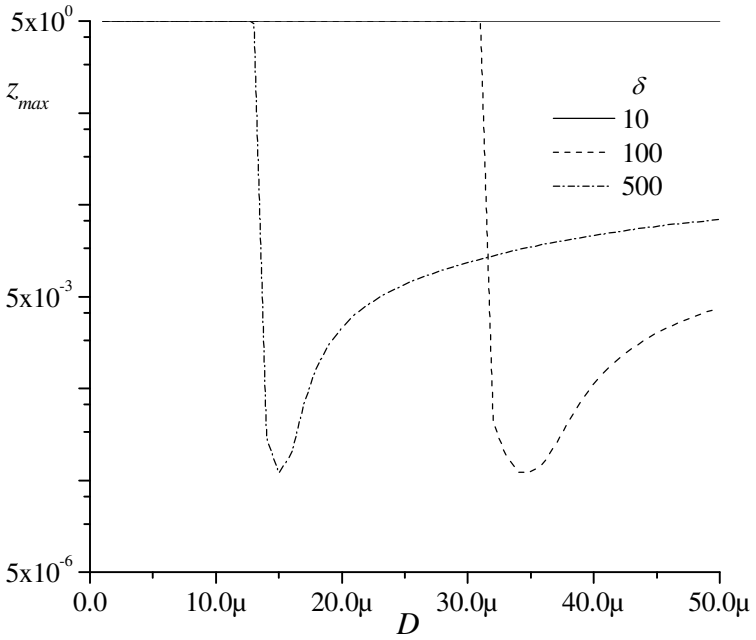

b)

Figure 5-8 Maximum radial and axial distances travelled by particles in a BDVE for different density ratios.

ratio is increased to 100, particles with radii greater than 32 µm start to move away from the inner vortex and impact the sidewall. However, when the density ratio is increased to 500 (see part (b) of Figure 5-8), particles with radii as low as 15 µm will contact the wall, and at the same time, cross a shorter axial distance when compared to lighter particles with density ratios of 10 and 100. Clearly, when the density ratio is increased, particles will have a higher moment of inertia that will compel them to gravitate towards the wall more rapidly. This explains why particles with a density ratio of 500 cross a shorter distance before striking the wall. One can therefore conclude that particle trajectories strongly depend on density ratio δ.

5.5 Effect of Initial Velocity (v)

The effect of varying the initial axial velocity of particles, $\boldsymbol{v}$ is studied by injecting a 25 µm particle at different dimensionless radial distances with axial velocities of 1, 10, and 100 m/s. Figure 5-9 shows that increasing the axial velocity does not have a noticeable effect on the maximum distance travelled by particles in the radial and axial directions. Moreover, as shown in part (b), when the initial velocity is increased, radius greater than 32 µm will initially move in the z-direction because of the higher particles with a velocity in the axial direction. However, they will eventually follow the same path as that of the particles injected with a lesser velocity. Therefore, because of the high tangential and axial velocities in a bidirectional vortex engine, the axial component of velocity of injected particles seems to have a minimal impact on particle trajectories.

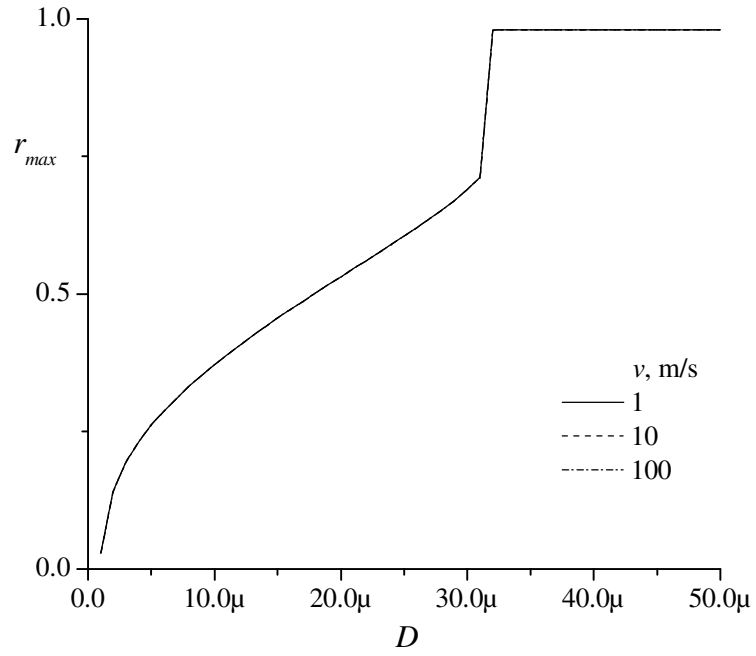

a)

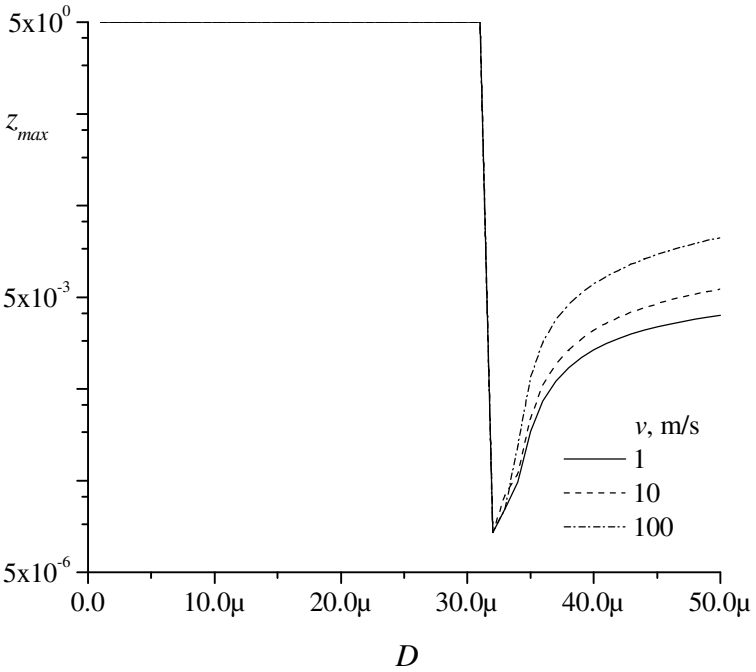

b)

Figure 5-9 Trajectories of different size particles of identical density originating at equidistant points taken along the radius of the combustion chamber with different initial axial velocities.

Chapter 6

Conclusion

In this study the various parameters that affect particle trajectories in solid rocket motors and bidirectional vortex engines are examined. In deriving the drag force, Stokes flow conditions are assumed and validated by calculating the relative Reynolds number for particles ranging in size from 10 to 500 μm in an idealized solid rocket simulation and 10 to 50 μm in a bidirectional vortex chamber. In the numerical simulations, drag, virtual mass, surface, lift and gravity forces are initially considered and, by performing an order of magnitude force analysis on a typical 100 μm and 25 μm particle in solid rocket motor and bidirectional vortex engine, respectively, the important forces affecting the particle trajectory are found to be almost exclusively drag and gravity in a solid rocket motor and drag only in a bidirectional vortex chamber. When particle distributions are plotted at a downstream axial distance of $z = 20$ in a solid rocket motor, smaller particles are shown to exit the combustion chamber near the axis of the motor, whereas larger particles are shown to exit near the combustion chamber sidewall. In a simulated solid rocket motor

the effect of the density ratio is seen to be negligible on trajectories followed by small-size particles with radii between 10 and 100 μm but important in the case of larger particles with radii greater than 100 μm.

In the bidirectional vortex engine, we study the effect of particle size, density ratio of particles with respect to the conveying medium, geometric inlet parameter, and initial injection velocity on particle trajectories. When injected at different radial positions, we find that smaller particles remain confined to the inner vortex, but heavier particles cross into the outer vortex before impacting the sidewall. The maximum radial and axial distances travelled by the particles is predicted as function of input parameters. Overall, we find that particles with higher density ratios travel a shorter axial distance before crossing into the outer vortex. They hence reach the sidewall more quickly. The parameter affecting particle motion most significantly are found to be the geometric inflow parameter, κ, particle size, and density ratio, δ. Decreasing the value of κ leads to a high local swirl velocity that causes, by virtue of centrifugal action, even the smallest of particles to gravitate away from the inner vortex, outwardly in the radial direction. The initial injection velocity seems to have a negligible effect on the radial and axial movement of particles so long as it remains small with respect to the tangential speed. We conclude that particle size, geometric inflow parameter and density ratio represent the three most important quantities affecting particle trajectory in a bidirectional vortex chamber.

References

[1] Chiaverini, M. J., Malecki, M. J., Sauer, J. A., and Knuth, W. H., "Vortex Combustion Chamber Development for Future Liquid Rocket Engine Applications," AIAA Paper 2002-2149, July 2002.

[2] Crowe, C., "The State-of-the-Art in the Development of Numerical Models for Dispersed Phase Flows," *Proceedings of International Conference on Multiphase Flows,* Vol. 3, 1991, pp. 49-60.

[3] Crowe, C., Sommerfeld, M., and Tsuji, Y., "Multiphase Flows with Droplets and Particles," CRC Press, 1998, pp. 27-29.

[4] Maxey, M. R., and Riley, J. J., "Equation of Motion for a Small Rigid Sphere in a Nonuniform Flow," *Physics of Fluids,* Vol. 26, No. 4, 1983.

[5] Wallis, G. B., *One-Dimensional Two-Phase Flow*, McGraw-Hill Companies, 1969, pp. 22-23.

[6] Kolev, N. I., "Multiphase Flow Dynamics Fundamentals," Springer, 2007, pp. 2-3.

[7] Anderson, T., and Jackson, R., "Fluid Mechanical Description of Fluidized Beds. Equations of Motion," *Industrial and Engineering Chemistry Fundamentals,* Vol. 6, No. 4, 1967, pp. 527-539.

[8] Pfender, E., "Fundamental Studies Associated with the Plasma Spray Process," *Surface and Coatings Technology,* Vol. 34, No. 1, 1988, pp. 1-14.

[9] Fuchs, N., Daisley, R., Fuchs, M., Davies, C., and Straumanis, M., "The Mechanics of Aerosols," *Physics Today,* Vol. 18, 1965, p. 73.

[10] Ingenito, A., and Bruno, C., "Using Aluminum for Space Propulsion," *Journal of Propulsion and Power,* Vol. 20, No. 6, 2004, pp. 1056-1063.

[11] Faeth, G., "Current Status of Droplet and Liquid Combustion," *Progress in Energy and Combustion Science,* Vol. 3, No. 4, 1977, pp. 191-224.

[12] Smith-Kent, R., Perkins, F., and Abel, R., "A Potential, Two-Phase Flow Model for Predicting Solid Rocket Motor Slag," AIAA Paper 1993-2307, January 1993.

[13] Boraas, S., "Modeling Slag Deposition in the Space Shuttle Solid Rocket Motor," *Journal of Spacecraft and Rockets,* Vol. 21, No. 1, 1984.

[14] Neilson, J. H., and Gilchrist, A., "An Experimental Investigation into Aspects of Erosion in Rocket Motor Tail Nozzles," *Wear,* Vol. 11, No. 2, 1968, pp. 123-143.

[15] Haloulakos, V., "Slag Mass Accumulation in Spinning Solid Rocket Motors," *Journal of Propulsion and Power,* Vol. 7, No. 1, 1991, pp. 14-21.

[16] Renie, J. S., Lilley, J. S., and Frederick, R. A., "Aluminum Particle Combustion in Composite Solid Propellants," AIAA Paper 1982-1110, June 1982.

[17] Horton, M. D., and McGie, M. R., "Participate Damping of Oscillatory Combustion," *AIAA Journal,* Vol. 1, No. 6, 1963, pp. 1319-1326.

[18] Price, E. W., "Experimental Solid Rocket Combustion Instability," *Proceedings of the Combustion Institute.,* Vol. 10, No. 1, 1965, pp. 1067-1082.

[19] Cai, W., Ma, F., and Yang, V., "Two-Phase Vorticoacoustic Flow Interactions in Solid-Propellant Rocket Motors," *Journal of Propulsion and Power,* Vol. 19, No. 3, 2003, pp. 385-396

[20] Hoekstra, A. J., Derksen, J. J., and Van Den Akker, H. E. A., "An Experimental and Numerical Study of Turbulent Swirling Flow in Gas Cyclones," *Chemical Engineering Science,* Vol. 54, 1999, pp. 2055-2065.
[21] Dring, R., and Suo, M., "Particle Trajectories in Swirling Flows," *Journal of Energy,* Vol. 2, 1978, pp. 232-237.
[22] Zhou, L., and Soo, S., "Gas-Solid Flow and Collection of Solids in a Cyclone Separator," *Powder Technology,* Vol. 63, No. 1, 1990, pp. 45-53.
[23] Chiaverini, M. J., Malecki, M. J., Sauer, J. A., and Knuth, W. H., "Vortex Combustion Chamber Development for Future Liquid Rocket Engine Applications," AIAA Paper 2002-2149, July, 2002.
[24] Fang, D., Majdalani, J., and Chiaverini, M. J., "Hot Flow Model of the Vortex Cold Wall Liquid Rocket," AIAA 2004-3676, July 2004.
[25] Brennen, C., *Fundamentals of Multiphase Flow*, Cambridge University Press, 2005.
[26] Batterson, J. W., Maicke, B. A., and Majdalani, J., "Advancements in Theoretical Models of Confined Vortex Flowfields," JANNAF Paper TP-2007-222 May 2007.
[27] Taylor, J., *Classical Mechanics*, University Science Books, 2005.
[28] Webster, A. G., *The Dynamics of Particles and of Rigid, Elastic, and Fluid Bodies*, 2nd ed., Merchant Books, 2006, p. 320.
[29] Acheson, D., *Elementary Fluid Dynamics*, Oxford University Press, New York, NY, 1990.
[30] Schiller, L., and Naumann, Z., "A Drag Coefficient Correlation," *Zeitschrift des Vereines Deutscher Ingenieure,* Vol. 77, 1935, pp. 318-320.
[31] Happel, J., and Brenner, H., *Low Reynolds Number Hydrodynamics: With Special Applications to Particulate Media*, Martinus Nijhoff Publishers, Hague, Netherlands, 1983.
[32] Stokes, S., "On the Effect of the Internal Friction of Fluids on the Motion of Pendulums," *Transactions of the Cambridge Philosophical Society,* Vol. 9, 1851, p. 8.
[33] Magnus, G., "On the Deviation of Projectiles; and on a Remarkable Phenomenon of Rotating Bodies," *Memoirs of the Royal Academy, Berlin*, 1852, pp. 210-231.
[34] Saffman, P., "The Lift on a Small Sphere in a Slow Shear Flow," *Journal of Fluid Mechanics,* Vol. 22, No. 2, 2006, pp. 385-400.
[35] Rubinow, S. I., and Keller, J. B., "The Transverse Force on a Spinning Sphere Moving in a Viscous Fluid," *Journal of Fluid Mechanics,* Vol. 11, No. 03, 1961, pp. 447-459.
[36] Rubin H. Landau, Manuel J. Páez, and Bordeianu, C. C., *Computational Physics: Problem Solving with Computers*, 2nd ed., Wiley-Interscience, 2007, p. 215.
[37] Forsythe, G. E., Malcolm, M. A., and Moler, C. B., *Computer Methods for Mathematical Computations*, Prentice Hall Professional Technical Reference, 1977, p. 259.
[38] Culick, F. E. C., "Rotational Axisymmetric Mean Flow and Damping of Acoustic Waves in a Solid Propellant Rocket," *AIAA Journal,* Vol. 4, 1966, pp. 1462-1464.

[39] Majdalani, J., and Akiki, M., "Rotational and Quasiviscous Cold Flow Models for Axisymmetric Hybrid Propellant Chambers," *Journal of Fluids Engineering,* Vol. 132, No. 10, 2010, pp. 101202-7.

[40] Majdalani, J., Private Communication, Corrected Solution of the Sidewall Boundary Layers of the Bidirectional Vortex, April 2011.

[41] Hoekstra, A. J., Derksen, J. J., and Van Den Akker, H. E. A., "An Experimental and Numerical Study of Turbulent Swirling Flow in Gas Cyclones," *Chemical Engineering Science,* Vol. 54, No. 13-14, 1999, pp. 2055-2065.

Vita

Ajay Katta received his B. Tech in Aeronautical Engineering from the Institute of Aeronautical Engineering, Hyderabad, India. His major area of interest was in Aerodynamics and Propulsion. His undergraduate project was entitled “Design of Bi-propellant Rocket Engine” and it involved the theoretical design of a liquid rocket engine using optimization theory. His predictions compared favorably with hot test results of a 200 kg thruster. Presently, he is pursuing his MS in Aerospace Engineering at The University of Tennessee Space Institute with Dr. J. Majdalani as a Graduate Research Assistant at the Advanced Theoretical Research Laboratory. His work with Prof. Majdalani is focused in the area of multiphase flows. He is the recipient of the 2006 Lloyd Crawford Fellowship.